



A 3D shear-wave velocity model of the upper mantle beneath China and the surrounding areas



Shantanu Pandey^{a,1}, Xiaohui Yuan^{a,*}, Eric Debayle^b, Keith Priestley^c, Rainer Kind^{a,d}, Frederik Tilmann^{a,d}, Xueqing Li^a

^a Deutsches GeoForschungsZentrum GFZ, Telegrafenberg, 14473 Potsdam, Germany

^b Laboratoire de Géologie de Lyon: Terre, Planètes et Environnement, Centre National de la Recherche Scientifique, Université Lyon, 1 et Ecole Normale Supérieure de Lyon, France

^c Bullard Laboratories, University of Cambridge, Cambridge, UK

^d Freie Universität Berlin, Germany

ARTICLE INFO

Article history:

Received 1 August 2013

Received in revised form 11 July 2014

Accepted 12 July 2014

Available online 22 July 2014

Keywords:

Rayleigh wave

Surface wave

Tomography

Fundamental mode

Higher modes

China

ABSTRACT

We present a three-dimensional model of shear wave velocity for the upper mantle of China and the surrounding region by analyzing 50,338 vertical component multi-mode Rayleigh wave seismograms, recorded at 144 permanent and more than 300 temporary broadband stations in and around China. The procedure involves combination of 1-D path average models obtained by modeling each Rayleigh waveform up to the 4th higher mode in a tomographic inversion scheme. The dense station network and the use of multi-mode analysis help to achieve a lateral resolution of a few hundred kilometers down to 400 km depth. The seismic lithosphere, as it is defined by the crust and the high velocity mantle lid, is to the first order thin in east China and thick in the west, with a high velocity lid extending down to about 200 km depth beneath much of the Tibet–Pamir plateau. Beneath India, the thickness of the seismic lithosphere gradually increases from ~100 km in south India to more than 150 km in north India, where it underthrusts the Tibetan plateau to approximately the Jinsha River Suture. High velocity lid extending down to 100–150 km depth is also observed in the Tarim basin, Sichuan basin and Ordos block. In the eastern part of the North China craton the seismic lithosphere is probably close to or thinner than 70 km. Adjacent to these areas, the high velocity lid in the eastern Yangtze craton and South China fold system extends down to 70–80 km depth. A large-scale subhorizontal high velocity body is observed at depths of 150–350 km beneath the entire east China cratonic areas. This high velocity body might be the remnant of a delamination process which resulted in the decratonization of the North China and the Yangtze cratons.

© 2014 Elsevier B.V. All rights reserved.

1. Introduction

China is an assembly of ancient continental fragments separated by fold belts, which were accreted from the late Proterozoic to the Cenozoic (e.g., Huang et al., 1980). Its present tectonics has been profoundly shaped by the Indo-Asian continental collision in the southwest and the subduction of the NW Pacific plate in the east with resistance by the Siberian shield in the north (Fig. 1). China has three major Precambrian cratons: the North China craton (NCC, also called Sino-Korean craton), the Yangtze craton (YC, also called South China craton) and the Tarim block. The interactions among different blocks have formed the tectonic features seen today and caused many intraplate earthquakes (Liu et al., 2007; Ma, 1987; Ma et al., 1984; Yin and Harrison, 2000). The convergence of Indian and Eurasian plates, which started 50 million years ago, has created the world's largest plateau

and is pushing the crust and mantle lithosphere out of its way to the east (e.g., Royden et al., 2008). The NW Pacific and Philippine Sea plate subduction zone produced substantial heterogeneity in the mantle beneath east China, as well as widespread uplift, volcanism and extension. North China and Mongolia comprise the major part of the Central Asian Orogenic Belt (CAOB), which was accreted from the Neoproterozoic to the Mesozoic due to the resistance of the Siberian shield (Windley et al., 2007). All of these events have left their imprint on the upper mantle structure. Unraveling the tectonic history and understanding the tectonic processes require a better knowledge of the China lithosphere.

High-viscosity lithospheric plates moving over a lower-viscosity asthenosphere are basic elements of plate tectonics. The terms lithosphere and asthenosphere were originally defined with reference to rheology, with the lithosphere essentially behaving as elastic solid, and the asthenosphere deforming as a viscous fluid (Barrell, 1914). Later on, additional terms like thermal, chemical or seismic lithosphere have been introduced (Anderson, 1995; Eaton et al., 2009), with the seismic lithosphere being defined as the high velocity lid overlying a low velocity asthenosphere. The bottom of the high velocity lid, and therefore the seismic lithosphere, can be defined as the point of inflection overlying

* Corresponding author.

E-mail address: yuan@gfz-potsdam.de (X. Yuan).

¹ Present address: AWI Bremerhaven, Am Alten Hafen 26, 27568 Bremerhaven, Germany.

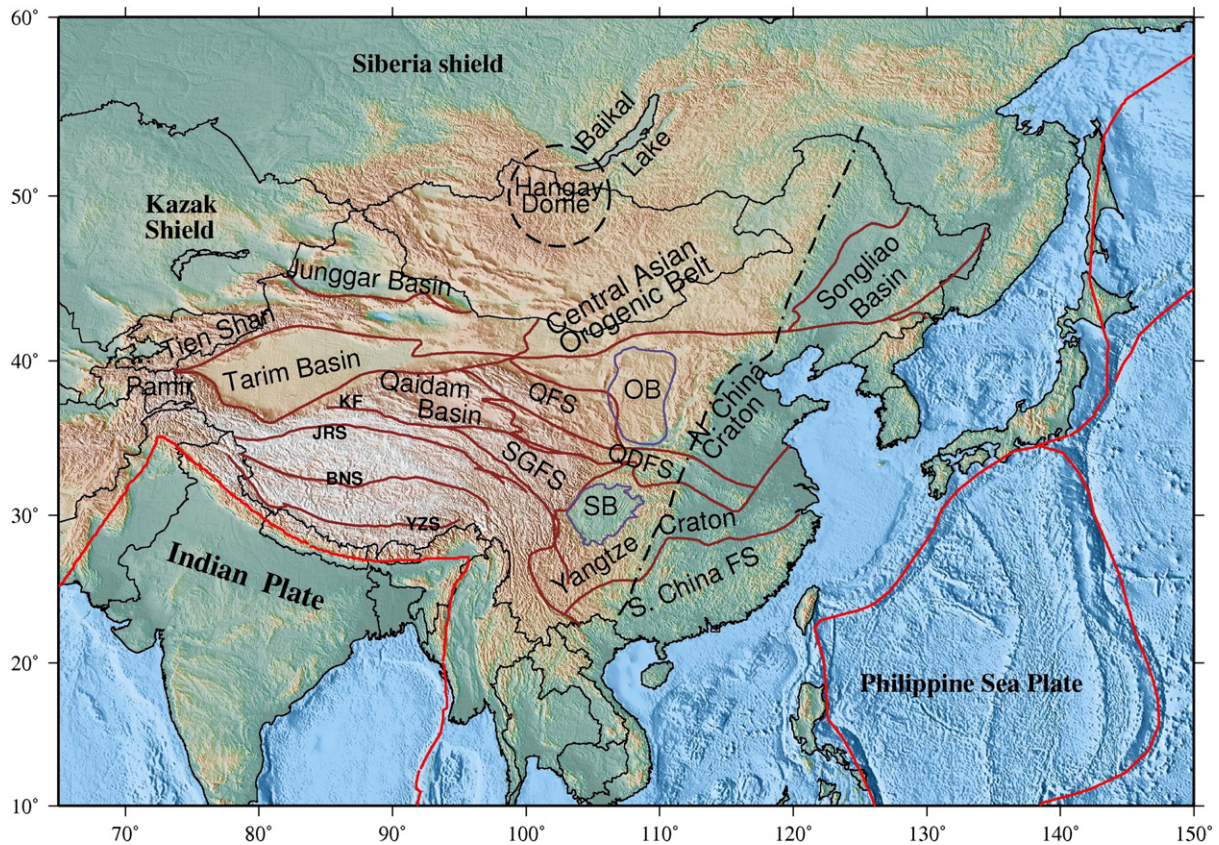


Fig. 1. Topography map of China and adjacent regions with major tectonic units. Red and blue lines define borders of major tectonic units. Black dashed line denotes the North–South Gravity Lineament (Xu, 2007). Abbreviation are: SGFS, Songpan–Ganzi fold system; QFS, Qinling fold system; QDFS, Qing–Dabie fold system; SB, Sichuan basin; OB, Ordos block; KF, Kunlun Fault; JRS, Jinsha–River suture; BNS, Bangong–Nujiang suture; YZS, Yarlung–Zangbo suture.

the low-velocity layer in the upper mantle velocity–depth relationship (Eaton et al., 2009). For the present work we adopt this definition.

Regional body wave tomography is sensitive to lateral variations but has poor vertical resolution in the shallow mantle, due to smearing along near-vertical propagation paths. The resolution normally begins at a depth roughly equal to the average inter-station distance. In contrast, the dispersion of surface waves provides a good vertical resolution (in general few tens of kilometers) of S-wave velocity. However, sampling continental upper mantle requires long period surface waves with typical path lengths greater than 2000 km (Li et al., 2008; Priestley and Tilmann, 2009; Sieminski et al., 2004), which limits horizontal resolution to at least a few hundred kilometers. In regional surface wave tomography, surface waves are often analyzed at periods shorter than 150 s, where the fundamental mode is mostly sensitive to the top 200 km. This sensitivity can be extended to a depth of more than 400 km by including higher modes (Debayle, 1999; Feng et al., 2010; Lebedev and Nolet, 2003; Priestley et al., 2006).

China is a very suitable place for surface wave study, as there are not only a lot of earthquakes in plate boundary zones around China, but also many intraplate earthquakes within China. Fundamental mode surface wave studies of China have reached a resolution of several hundred kilometers showing features correlated with the large geological units (Curtis et al., 1998; Feng and An, 2010; Friederich, 2003; Griot et al., 1998; Huang et al., 2003; Ritzwoller and Levshin, 1998; Romanowicz, 1982). These studies generally agree that the lithosphere reaches a thickness of more than 200 km in western China and thins to less than 100 km in eastern China. However, there are differences at a more regional scale. For example, Griot et al. (1998) and Huang et al. (2003) observed a thick lithosphere beneath the Tibetan plateau, while others reported on a thin mantle lid (Romanowicz, 1982) or a missing lithosphere (Friederich,

2003) beneath central and northern Tibet. The resolution can be improved by including surface wave overtones and by increasing the station density. Feng et al. (2010), Lebedev and Nolet (2003) and Priestley et al. (2006) have shown that the upper mantle structure of eastern Asia can be better constrained by fitting multi-mode surface waveforms, although they have only used few stations in China for which waveform data were available. Here we follow the approach used in Priestley et al. (2006) and apply the multi-mode surface wave tomography to 47 evenly spaced permanent broadband stations in China, for which the instrument response is well known. In order to increase the number of stations available we also used all publicly available temporary experiment data in China. The increased number of stations makes the inter-station spacing less than 300 km in east China (Fig. 2). The use of Rayleigh waves analyzed at periods longer than 50 s for path lengths greater than a few thousands of kilometers provides a lateral resolution of several hundred kilometers extending to a depth of 400 km.

In the present work we have performed both isotropic and anisotropic inversions. The isotropic components in both cases are very similar. We discuss here the isotropic component of the anisotropic inversion because it is less subject to biases. There is a few percent of azimuthal anisotropy in the uppermost 200 km. Interpreting the anisotropic pattern requires intensive resolution tests and will be done in another paper.

2. Data and methods

Our data comprise Rayleigh waves in vertical component seismograms. We utilize the fundamental mode and overtones up to rank 4. Fig. 3 shows the sensitivity kernels of the Rayleigh-waves of different modes and at different periods. While the fundamental-mode Rayleigh

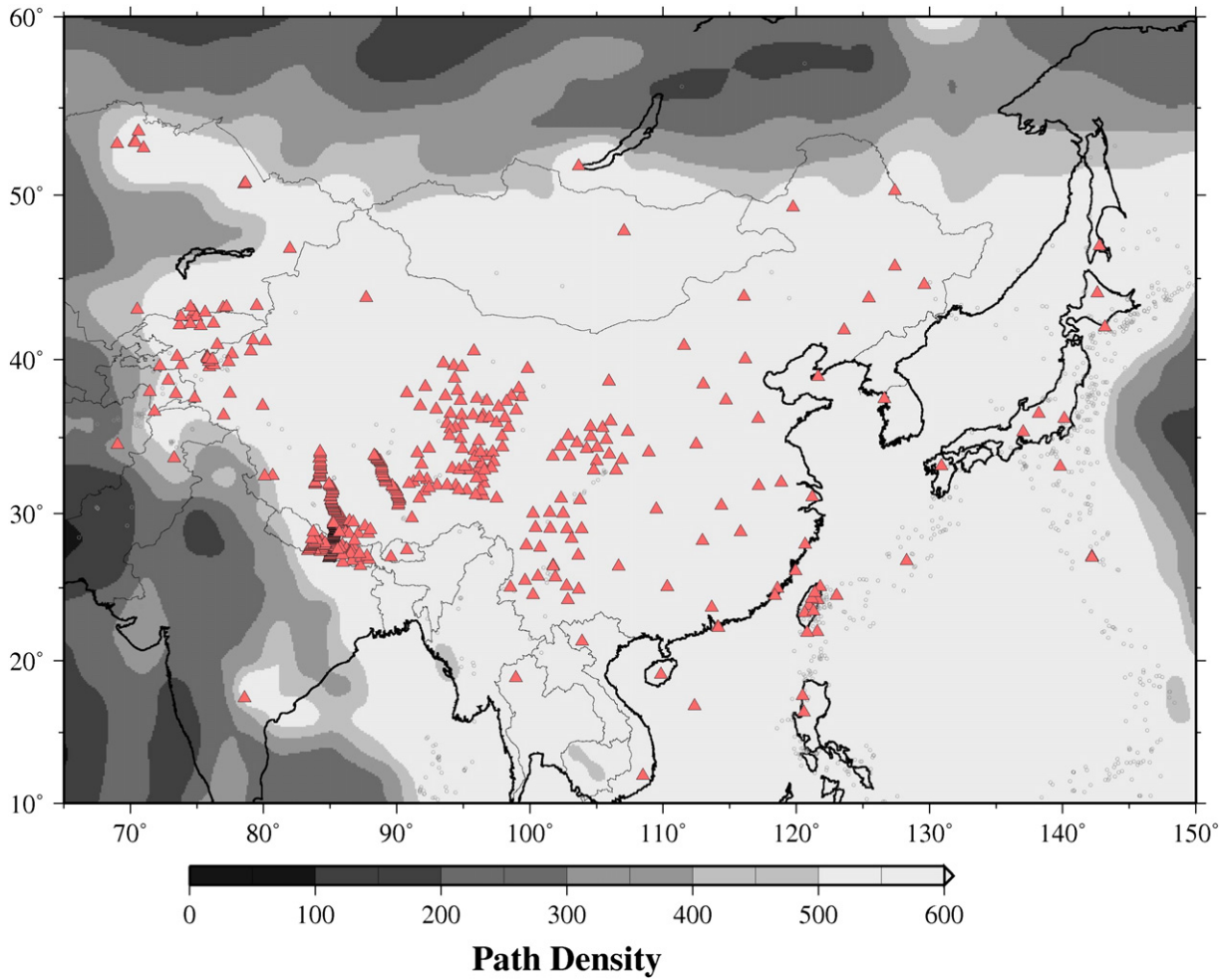


Fig. 2. Map of stations and ray coverage. Triangles denote the seismic stations used in the study. The path density is defined by number of paths crossing a grid of $2^\circ \times 2^\circ$.

waves theoretically exist for all frequencies, the higher modes are limited to higher frequencies. It can be seen that the sensitivity of the fundamental mode is generally limited to the upper mantle, whereas the

higher modes provide additional sensitivity below the mantle transition zone. Note that Fig. 3 is based on a theoretical calculation using a PREM model modified to remove the low velocity layer (Priestley

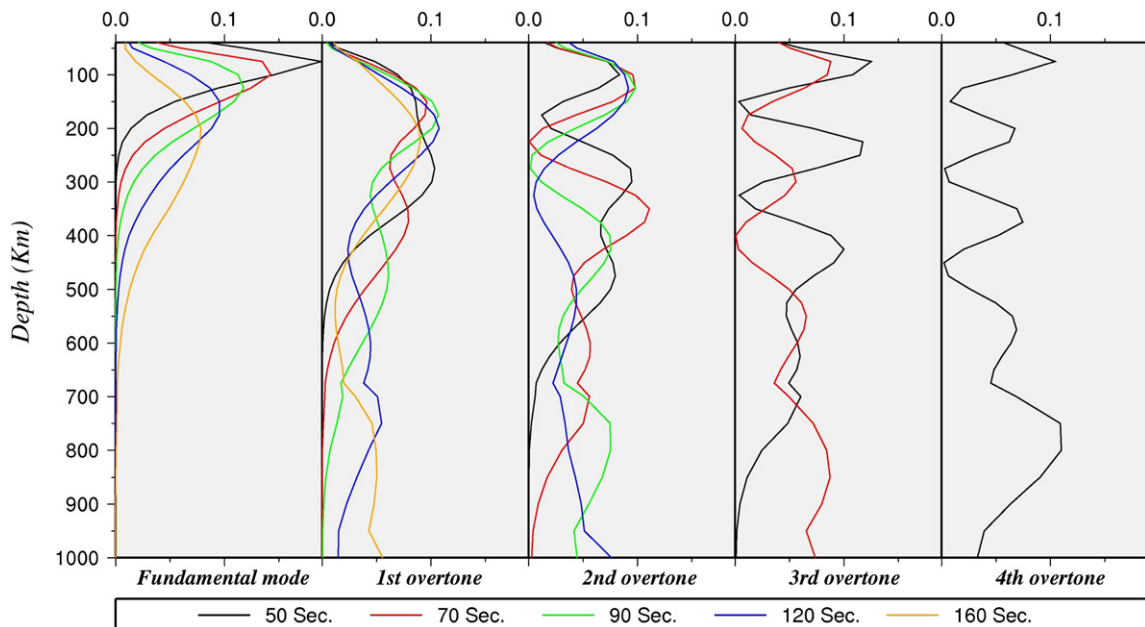


Fig. 3. Rayleigh wave sensitivities as a function of depth at different periods for the fundamental and the first four higher modes.

et al., 2006). The depth sensitivity of the observed data can be reduced by diverse factors such as missing frequency content, lack of higher mode excitation, mode conversion due to sharp lateral velocity contrasts and regularization of the inversion.

Waveform data from more than 400 stations (Fig. 2), which have been operational at some time between 1999 and 2007 have been requested from different agencies. We requested waveform data of 47 broadband stations from the Chinese Earthquake Network Center, many of which have not previously been used for this kind of study. In addition, data from more than 300 temporary stations in China and nearly 100 stations around China were requested from the IRIS and GEOFON data centers. The selected distribution of stations helped in achieving a good path coverage and azimuthal distribution (Fig. 2).

The technique used for constructing a 3D S_v model proceeds in two distinct stages. It was previously employed in a number of regional scale surface wave tomography studies (e.g. Debayle, 1999; Debayle and Kennett, 2000; Heintz et al., 2005; Pilidou et al., 2004; Priestley et al., 2006).

2.1. Waveform inversion for a path-average 1D model

In the first stage we model each waveform by a 1D shear wave velocity model representing an average seismic structure from a source to a receiver. We use the automated version (Debayle, 1999) of the waveform inversion approach of Cara and L ev eque (1987). An original aspect of this approach is the introduction of a set of secondary observables, built up from the waveforms as the primary data of the inversion. Compared to the strongly nonlinear problem of inverting for waveforms directly, these secondary observables have only a mild nonlinear dependence on the model parameters. This property minimizes the dependence on the starting model and reduces the number of iterations needed to find a 1D depth-dependent model, which predicts waveforms compatible with the observed surface wave seismogram. In detail, the observed vertical component data are cross-correlated with pure-mode synthetics computed for a reference model for the fundamental and four higher modes. The resulting cross-correlograms are filtered at different frequencies using Gaussian filters, and then their envelope function is calculated. A set of secondary observables is then selected by sampling values taken at different time lags on the envelope on each of the actual cross-correlograms: one value at each significant local maximum of the envelope function and two values on the flanks of those maxima. The automated selection of these secondary observables is discussed in details by Debayle (1999) and Debayle and Ricard (2012). The waveform inversion matches these secondary observables with synthetic secondary observables. Once the envelope-based secondary observables are fitted, the inversion proceeds by fitting the phase of the cross-correlogram at the maximum of the envelope function. The cross-correlation with pure-mode synthetics obviates the need for explicit mode separation of the observed data and the automated selection of secondary observables makes the inversion scheme robust in the case of a mode being insufficiently excited or strongly overlapping with another mode.

This approach requires two basic assumptions that the observed seismograms can be represented in terms of multi-mode surface waves that propagate independently and that they do so along great circle paths. The necessary condition for the validity of the first assumption is that the medium should be varying smoothly (Woodhouse and Jun, 1974) and for the second that the lateral velocity variations should not be too large. Kennett (1995) finds that the validity of the path-averaged approximation holds good at period greater than 30 s and for surface waves propagating beneath continents at regional distances (with typical path lengths of $< \sim 4000$ km). For the case where surface waves cross major structural boundaries (continent–ocean transition) he suggests to use the path-average approximation only at periods greater than 50 s. In addition, results from other studies (Trampert and Woodhouse, 1995; Yoshizawa and Kennett, 2002) show that for

the fundamental and first higher modes, off-great circle propagation can be neglected at periods greater than 40 s and at epicenter-station distances smaller than 10,000 km. For these reasons, and considering the large variation in crustal thickness, with extremely thick crust in Tibet and a thinner oceanic crust at the margins of the study region, we choose to process surface waves in the period range 50–160 s. Removing the shortest periods (< 50 s) reduces the effect of strong lateral variations in the shallow part. By limiting our analysis to long period surface waves, we can work safely with the great circle approximation and expect that propagation or site effects can be neglected.

The waveform fitting procedure is automatic for each seismogram. The period range used here is 50–160 s for the fundamental and up to four higher Rayleigh wave modes, depending on their signal-to-noise ratio (SNR). At each period, the SNR is deemed adequate if the ratio between the maximum amplitudes of the envelopes of the signal and noise is greater than 3. The signal is evaluated in five bandwidths centered at periods of 50, 70, 90, 120, and 160 s. The inversion is performed for the upper mantle structure with the crustal structure being fixed. We used path average crustal models from the 3D global 3SMAC crustal model (Nataf and Ricard, 1995) and the smoothed PREM model for the mantle and compute the stress displacement functions necessary to build the initial synthetic seismograms using the code from Takeuchi and Saito (1972). Source parameters are taken from the Global CMT catalog. The inversion is considered successful if the final synthetics matches well the observed seismogram and if the inversion converges towards a unique and stable velocity model (Debayle, 1999). Debayle (1999) uses a chi-square misfit parameter to ensure that the secondary observables are well fitted. In addition, to make sure that the final model provides a good fit to the actual seismogram, he computes $E_{res/act}$, the energy of the residual signal over the energy of the actual signal, and Re , the energy reduction of the residual signal between the initial and last iterations. These energies are summed over the signal for group velocities between 3.5 and 6 km/s. The inversion is considered successful if the misfit parameter is smaller than 3 and if $E_{res/act} < 0.3$ or $Re > 90\%$. The output of this inversion scheme is a 1-D path average shear wave velocity model along each great circle path. In this study we obtained 50,338 1D path averaged models. Fig. 4 shows the distribution of path lengths. For this data set we achieved more than 100 paths crossing each 2° by 2° for the entire study area, and more than 500 paths almost everywhere in China (Fig. 2).

One half of the rays have path length shorter than 6000 km (Fig. 4). We also included paths longer than 6000 km in the study to increase ray coverage, although longer paths involve larger Fresnel zone and are more susceptible to off great-circle deviations and multi-pathing. We tested this effect by repeating the entire analysis by either using only shorter paths (< 6000 km) or using all paths and found that the bias due to longer paths is not recognizable (see Figs. S1 and S2). Comparison of Figs. 8 and S2 shows that the effect of longer paths is small and does not affect the interpretation of our tomographic model. Our preferred model is the one that include longer paths, as we believe that the benefit of the additional ray coverage is greater than the bias due to off-great circle propagation.

Because of the imposition of the a priori crustal model, anomalies above the Moho are not constrained by the surface wave data but simply reflect the a priori model. Anomalies immediately below the Moho are in principle resolved, but will suffer from significant artifacts if there are discrepancies between the actual and assumed crustal structures. This trade-off has been evaluated by Debayle and Kennett (2000) and Priestley et al. (2006), and is likely to be small at depths greater than 100 km.

In Fig. 5 we show examples of the waveform inversion for four selected paths. The phase of the surface waveforms has been matched very well for paths 1, 2, and 4. For path 3 the delay in the fundamental wave mode is still slightly underpredicted because the regularization discourages extreme changes to the reference model, and an error bar of 5% is used on the phase of the cross-correlogram function (Debayle,

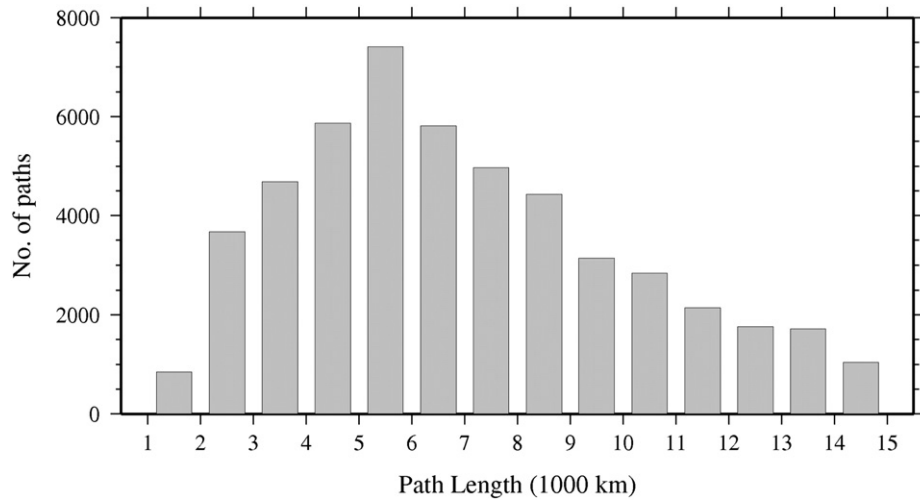


Fig. 4. Histogram of path lengths in the final dataset.

1999), allowing a slight misfit between the observed and synthetic waveform. In fact, path 3 represents the worst case of the selected waveforms that is just at threshold of the acceptance. The amplitudes are not quite as well matched, as these depend more strongly on three-dimensional structure, and therefore cannot be matched perfectly by a 1D pure path inversion. For path 4 only changes in the upper 200 km of the model are required to fit the waveform data, while deeper portion of the models was modified by the inversion for the other paths.

2.2. Tomographic inversion

In the second stage we combine the 1-D velocity models in a tomographic inversion using a scheme developed by Debayle and Sambridge (2004) for massive datasets. This scheme is an extension of the continuous regionalization algorithm of Montagner (1986) using the inversion approach of Tarantola and Valette (1982). This algorithm produces both the isotropic component of 3D Sv-wave speed heterogeneity and the azimuthal anisotropy. A laterally smooth model is obtained by imposing correlation between neighboring points with the use of a Gaussian covariance function. Indeed, the Tarantola and Valette (1982) approach can be seen as a way of finding the model that gives the best fit to the data while keeping it as “close” as possible to the a priori information. The smoothness of the inverted model in poorly sampled regions is therefore mostly constrained by the width of the Gaussian covariance function, while in regions with higher ray density the need for a satisfactory data fit allows a rougher model. The Gaussian covariance function between two points r and r' is:

$$C_{mo}(r, r') = \sigma_r \sigma_{r'} \exp\left(-\frac{\Delta_{r,r'}^2}{2L_{corr}^2}\right),$$

where $\Delta_{r,r'}$ is the distance between r and r' , σ_r is the standard deviation in point r and L_{corr} is the correlation length (Montagner, 1986). L_{corr} controls the horizontal smoothness of the model and σ_r controls the amplitude of the model perturbation at a geographical point r . The Earth model is discretized in 1° by 1° cells, which is much smaller than the surface wave wavelength or Fresnel zone at our period of interest. Although the inversion problem is strongly underdetermined (the number of independent pieces of information contained in the data is less than the number of model parameter), the inversion problem is stabilized by the use of appropriate regularization. A reasonable way to choose L_{corr} is to make sure that the surface of width $2L_{corr}$ centered around each of the ray

paths ensures a good coverage of the study area. With our dataset, this condition is fulfilled, even when L_{corr} corresponds to the shortest wavelength (~ 200 km for 50 s Rayleigh waves). After several trials, we set L_{corr} to 250 km. This value allows us to exploit the information contained in our shortest period Rayleigh waves (Sieminski et al., 2004), while keeping a relatively smooth model. Following Debayle and Sambridge (2004) and Montagner (1986), we argue that the choice of L_{corr} , which is based on the data wavelength, is more physically based than choosing damping parameters in a classical inversion scheme. We show in Fig. S10 the effect of changing L_{corr} to 400 km. Although we obtain a smoother model, the large scale structures that are discussed in this paper are preserved. The a priori standard deviation is set to $\sigma = 0.05$ km/s according to the expected values at regional (Debayle and L ev eque, 1997; Debayle et al., 2001; Nishimura and Forsyth, 1989) and global scales (Debayle and Ricard, 2012). Following Debayle and Sambridge (2004) and Montagner (1986), we argue that the choice of L_{corr} , and of the a priori standard deviation, which are based on the data wavelength and on previous observed shear wave heterogeneities, is more physically based than choosing damping parameters in a classical inversion scheme.

In the next sections we will discuss the reliability of the model using different tests before presenting and discussing the preferred model.

3. Resolution tests and reliability of the model

In stage one of calculating 1D path-average model, artifacts can arise from errors in the assumed crustal model and source parameters. Synthetic tests in prior work suggest that the effects of crustal corrections with different crustal models, e.g., the 3SMAC or the CRUST2.0 (<http://igppweb.ucsd.edu/~gabi/rem.html>), are indistinguishable at depths larger than 100 km and are minor at shallower depths (Debayle and Kennett, 2000; Pilidou et al., 2004; Priestley et al., 2008b). In addition, a good (redundant) path density and azimuthal coverage like what we have for this work is a basic requirement for reducing the influence of errors in source parameters. Cara and L ev eque (1987) already demonstrated the weakness of the dependence on the reference model, so that we can safely start the inversion from a unique upper mantle model (a smooth version of PREM) with a crustal part adapted to each path.

For the second stage of determining the 3D model using a continuous regionalization scheme, we computed the a posteriori error on the tomographic model, using the formalism of Tarantola and Valette (1982) adapted to the continuous regionalization by Montagner

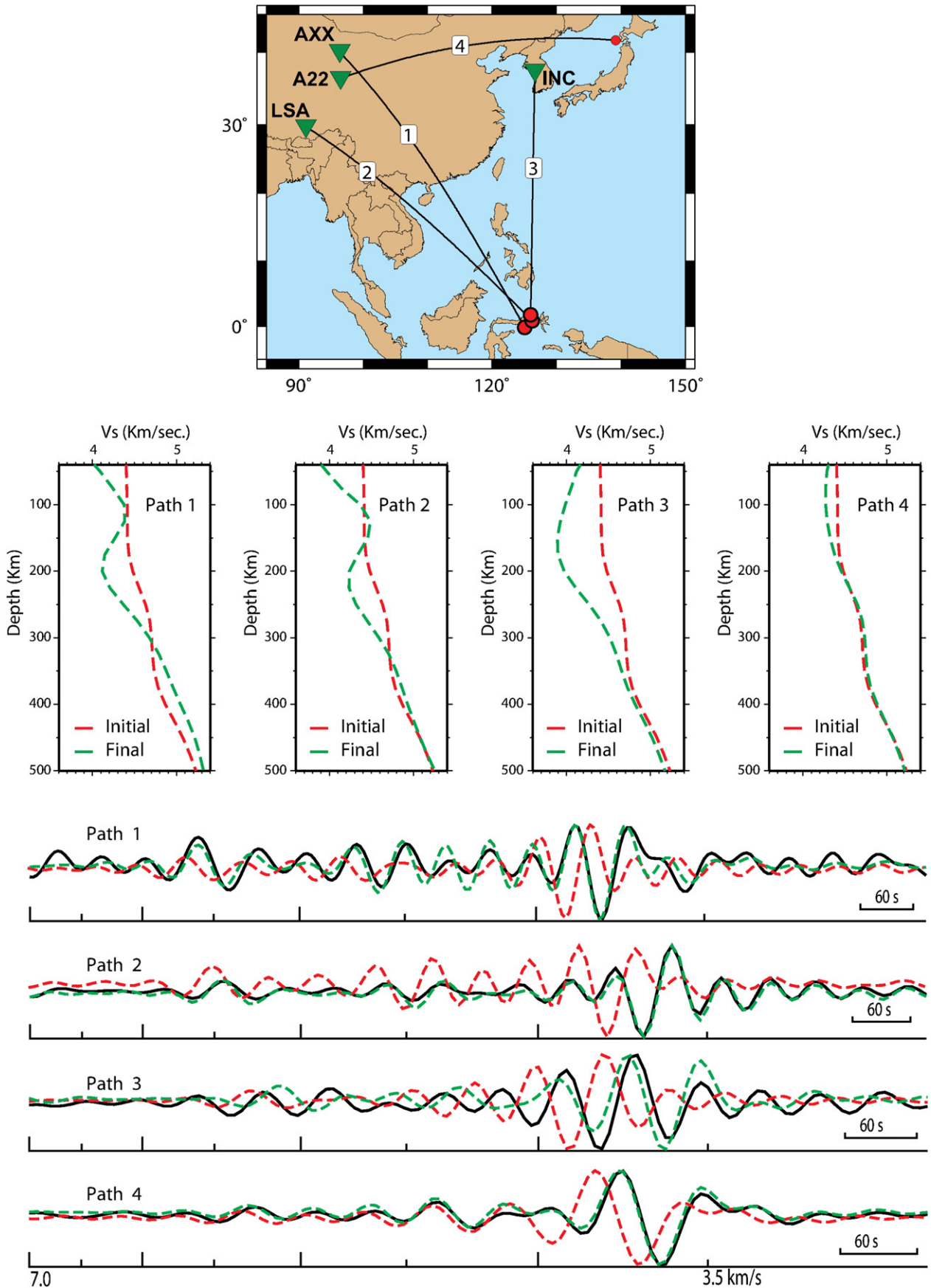


Fig. 5. Example of waveform inversion for 4 paths. Locations of the paths are indicated in the upper panel. The middle panels show the initial (red) and final (green) models. Waveforms are shown in the lower panels. Black curves are observed data, bandpass filtered within 50–160 s. Red and green curves are synthetic waveforms for the initial and final models, respectively.

(1986). Maps and cross sections in the 3D distribution of the a posteriori error are shown in Fig. 6. It is well known that the a posteriori error, which is obtained from the square root of the diagonal terms of the a posteriori covariance matrix, is a useful tool in order to quantify model resolution. The a posteriori covariance matrix C_m is related to the a priori covariance matrix C_{m0} by $C_m = (I - R)C_{m0}$, where I is the identity matrix

and R is the resolution matrix. Therefore, the error estimates depend on the a priori covariance matrix. We note that it is also true for R , and any resolution test will depend on the choices made for the correlation length and a priori standard deviation. Providing that our a priori choices are reasonable, the a posteriori errors are a very useful tool to guide the interpretation of the seismic model. Regions where the a posteriori error

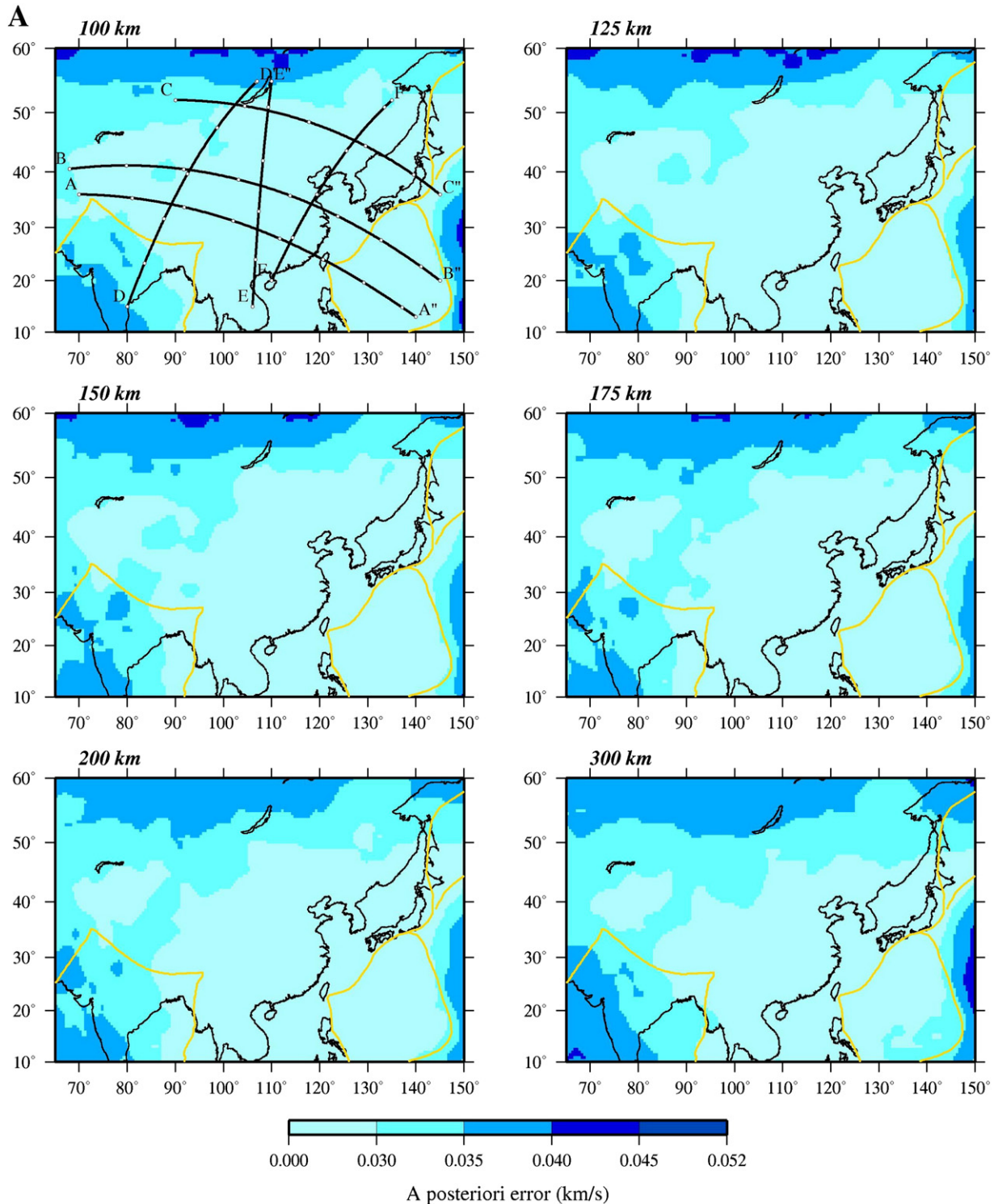


Fig. 6. A posteriori error map showing the (A) horizontal sections for depths of 100, 125, 150, 175, 200 and 300 km and the (B) vertical sections along the same profiles as shown for the model. The a posteriori error values are less than 0.035 km/s for most of the region (compare the a priori value of 0.05 km/s).

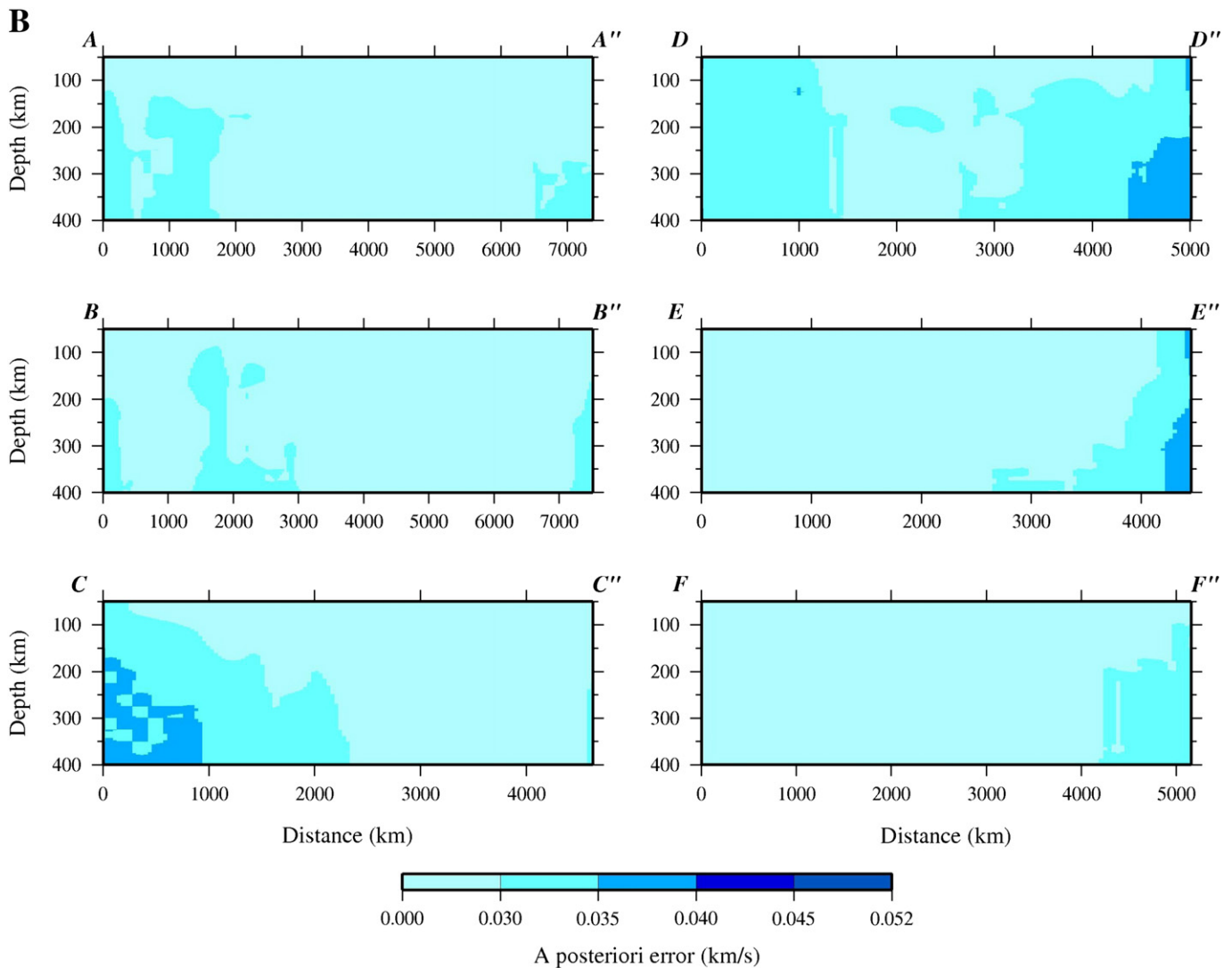


Fig. 6 (continued).

is close to the a priori error (i.e. $\sigma = 0.05$ km/s) can be regarded as the regions of poor resolution (R close to 0). Due to the dense path coverage and the presence of higher modes, the a posteriori error value is less than 0.035 km/s for the entire study region. This means that S-wave perturbations larger than ± 0.035 km/s ($\sim 0.8\%$ considering an average velocity of 4.4 km/s) are significant at the 68% confidence level and that perturbations greater than ± 0.07 km/s ($\sim 1.6\%$) are significant at the 95% confidence level. We indicate the 0.8% and 1.6% contour levels on the cross-sections (Figs. 9 and S5) as visual guide to areas of significant heterogeneity at 68% and 95% confidence levels, respectively. As the a posteriori error is actually smaller than 0.035 km/s in many parts of the study region (Fig. 6), these contours represent a conservative estimate.

For the second stage we checked the dependence of the results on the a priori and starting models (note that the a priori and starting models are identical) with a simple analytical test (flat model resolution test). We built two input synthetic models by adding a uniform shear wave perturbation of 5% and 15% to the a priori model and performed 3D tomographic inversions in order to recover these two synthetic models (Fig. S9). From the output, it is evident that our a priori choices ($L_{\text{corr}} = 250$ km; $\sigma = 0.05$ km/s) allow us to retrieve the flat model uniformly for the area of interest. In Fig. S9, we color in white a very

narrow interval (approx. 1%) around the target value of the model. The smearing around the edges of the map can be interpreted as the effect of the width of the Gaussian correlation length.

The image resolution is not so easy to quantify, but the checkerboard tests can provide a qualitative measure of our ability to resolve a particular input model. We conducted a number of checkerboard tests to examine the ability of the selected data set to recover velocity anomalies of different sizes. Fig. 7 shows the test with seismic anomalies extending over 500×500 km in the middle of the map horizontally and 100 km vertically. Alternating high and low velocity anomalies with magnitudes of $\pm 6\%$ are spread over the entire volume, separated by ~ 500 km wide zero percent anomalies. We calculated synthetic Rayleigh wave seismograms for the same ray paths, source parameters, and frequency contents as in the observed data and carried out the same inversion procedure. At shallow depth (< 200 km) the input model can be almost completely recovered. At depths of 200–400 km nearly half of the magnitude of the anomalies can be recovered. The synthetic test shown in Fig. 7 gives an intuitive representation of our ability to recover a particular model from our ray coverage and a priori choices at the scale length of the individual blocks. However, as shown by L ev eque et al. (1993) such a test does not demonstrate that other synthetic models with larger size structure will necessarily

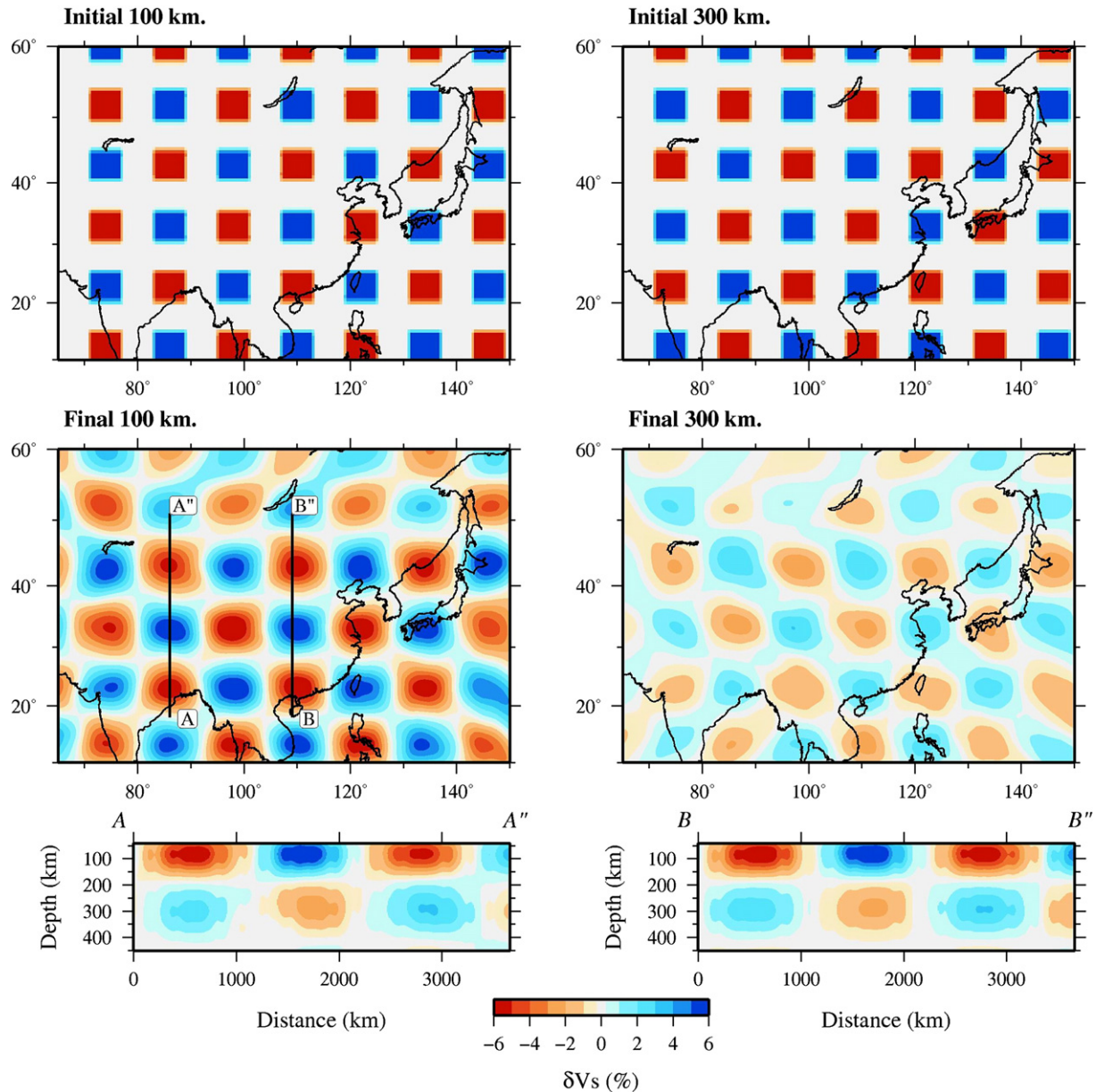


Fig. 7. Horizontal and vertical slices of the checker board resolution test. Alternating high and low velocity perturbations with a size of 500×500 km in horizontal and 100 km in depth and a magnitude of 6% are separated by zero-anomaly background in the input model.

be, or even equally well, retrieved. For this reason, we performed a further synthetic test with checker dimension of 1000×1000 km horizontally and 100 km vertically (Fig. S8). The geometries of these larger scale anomalies are also well retrieved. We therefore assume that seismic anomalies larger than 500 km in the horizontal direction and 50–100 km in the vertical direction are reasonably well resolved by our data in the uppermost 400 km.

The study area is very heterogeneous with dramatic variations in crustal thickness (Li et al., 2006; Zhang et al., 2011). Beneath the orogenic belts of Tibet, Tien Shan and Pamir the maximum crustal thickness reaches more than 80 km, measured by different seismic means (e.g., Kind et al., 2002; Li et al., 2006; Zhang et al., 2011). At shallow depth (less than 100 km) the 3D inversion may be affected by errors in our a priori knowledge of the crust. The strongest biases are expected in regions with the thickest crust. To test the effect of the thick crust we have removed the paths that cross a rectangular area in

western China where the crustal thickness is mostly over 60 km (mainly Tibet–Pamir–Tien Shan orogenic belts, see Fig. S3) and repeat the tomographic inversion. This results in 51% of all paths being removed, leading to a dramatic loss of coverage west of $\sim 105^\circ$, and of course a total loss of information in the excluded area. We display maps between 50 and 150 km depths in Fig. S4 and two vertical sections EE'' and FF'' in Fig. S5 which can be compared with Figs. 8 and 9. The eastern part of the maps at 100 and 150 km depths is very similar to the final model (Fig. 8) inverted using the entire dataset. Comparison of Figs. 9 and S5 demonstrates that the anomalies resolved at the 68% and 95% confidence levels have a very similar shape indicating that Sv velocity perturbations are robust in this part of the model, not significantly biased by paths crossing regions with thick crust and robust against a removal of about half of our dataset. The large scale pattern of sections EE'' and FF'' (Fig. 9) is also preserved after the inversion with the reduced data set. In particular, high velocity anomalies are visible beneath the Ordos

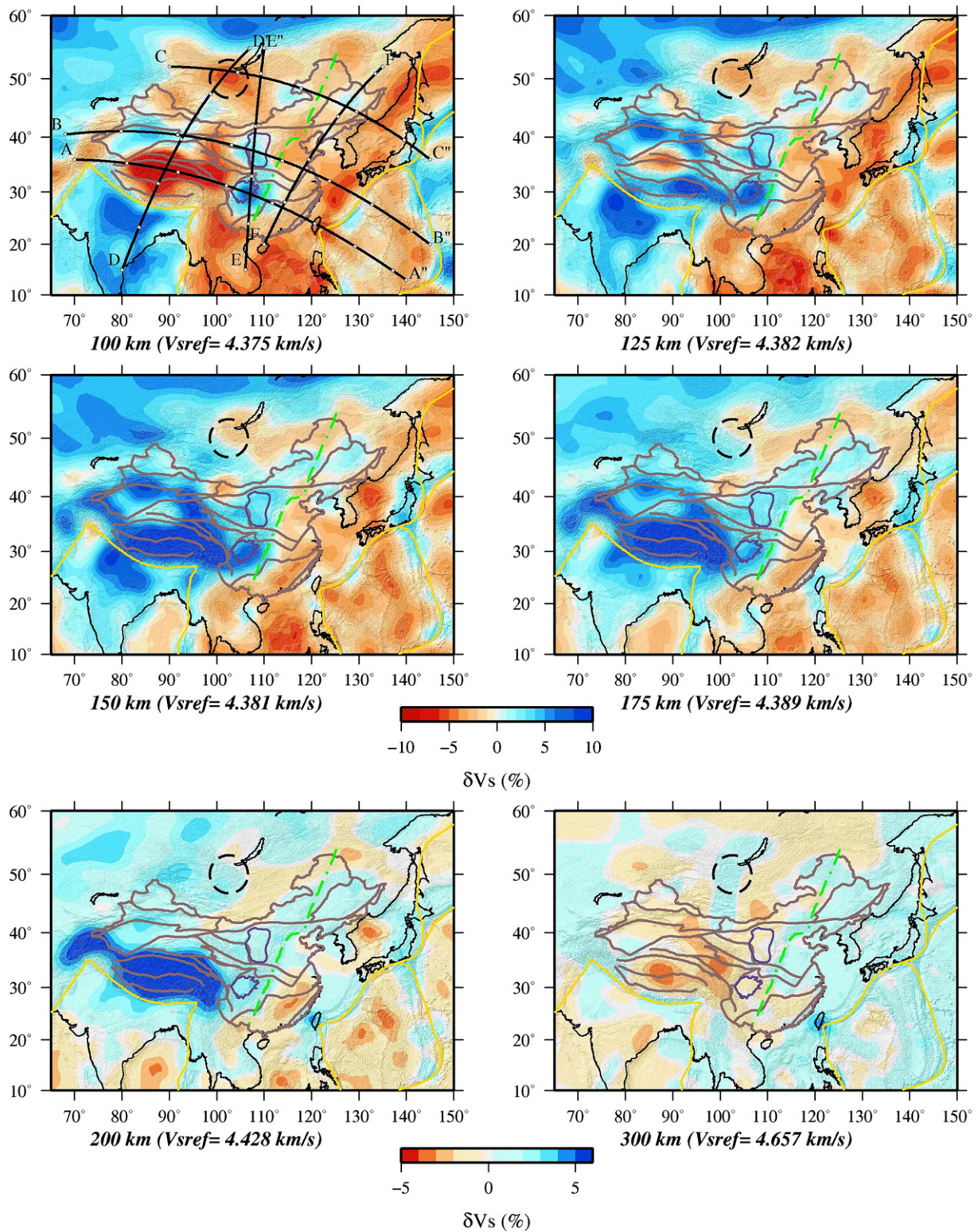


Fig. 8. Horizontal sections of the Sv-velocity perturbations at depths of 100, 125, 150, 175, 200 and 300 km. The percentage anomalies for depths of 100–175 km and for depths of 200–300 km are denoted by different scales. Where the crust is thicker than about 60 km in the 3SMAC model, the perturbations in the 100 km slice partly reflect the starting model. Locations of the 6 profiles shown in Fig. 9 are indicated on the map at 100 km depth. Gray lines mark borders of major tectonic units from Fig. 1. Green dashed line denotes the North-South Gravity Lineament.

block and Sichuan basin (from sub-crustal depth to >200 km), the Songliao basin (at >100 km depth) and for the South China fold system (thin lithosphere at <75 km depth).

Previous tests based on the same approach to waveform fitting (e.g. Priestley et al., 2008b) suggest that even beneath Tibet, the influence of a fixed crust is likely to be small at depths larger than 100–125 km.

4. Observations

4.1. Horizontal sections

Fig. 8 shows the 6 horizontal sections of the isotropic S_v velocity perturbations of the 3D inversion at depths from 100 to 300 km.

The slice at 100 km depth shows high velocities in India, Tarim basin, Sichuan basin, Ordos block and Songliao basin and wide-spread low velocities elsewhere including Tibet, the CAOB and in the oceanic areas. In the northwest Pacific subduction zones the low velocity anomalies following plate boundaries should represent the mantle wedges. In the depth range of 100–200 km we can recognize the downgoing slab by high velocities. The west China and CAOB are characterized by low velocity anomalies at shallow depths. At 100 km depth, the low velocity anomaly in Tibet is sharply bounded by the Indian plate to the south, by the Tarim basin to the north and by the Sichuan basin and Ordos block to the east, which show up as high velocity anomalies typical of continental lithospheric mantle. The low velocities in the central part likely arise due to a combination of a too low crustal thickness in the a priori model and possibly low velocities in the shallowest upper mantle in northern Tibet.

S wave anomalies at 125–200 km depth largely reflect the variation in the thickness of the seismic lithosphere. High velocity anomalies indicate the presence of mantle lithosphere. Low velocities are mainly associated with the asthenosphere. In general west China including Tibet, Tien Shan–Pamir, Sichuan basin, and Ordos block is characterized by thick lithosphere while the lithosphere beneath east China is thin. The high velocity anomaly in the mantle lithosphere beneath much of Tibet and the Pamirs extends to a depth of 200 km. At 125 km a low velocity zone can be observed in northeastern Tibet, focused along the western Kunlun Fault (KF) and Jinsha River Suture (JRS) south of Tarim and Qaidam basins. At the same location reduced velocities (slow compared to their immediate surroundings, not relative to the reference model) can be discerned to a depth of 175 km. North central India has high velocities down to a depth of 150 km, while high velocities beneath the rest of India can only be seen to shallower depth (<125 km). The Songliao basin in NE China also has high velocities.

The amplitude of S wave anomalies reduces significantly at depths below 200 km. However, the resolution tests also indicate that the magnitude of recovered anomalies is reduced by about 50%, such that the real change in the magnitude of anomalies is hard to quantify. In marked contrast to the structure at 150–200 km depth, low velocity asthenosphere dominates Tibet and the surrounding orogenic regions (e.g. Tien Shan). These low velocities appear to be surrounded by a (partially broken) ring of higher than average velocities. At 300 km depth high velocity is widespread in east China in a large area west of the Pacific subduction zone. The Pacific subduction zone including Taiwan and Japan is characterized by high velocity anomalies.

4.2. Vertical sections

We created 6 vertical sections crossing major tectonic units (Fig. 9). Sections AA", BB" and CC" are approximately in the east–west direction, while sections DD", EE" and FF" are in the north–south direction. Locations of the sections are indicated on the 100 km depth horizontal map in Fig. 8. For each section we plotted S velocity perturbation as well as the absolute velocity. Seismic anomalies depend on the reference model, and features such as low velocity zones (i.e. negative velocity gradients with depth) are more readily identified on absolute velocity profiles but smaller anomalies can be more easily identified in the perturbation image, such that both types of representation are complementary.

Section AA" extends from southernmost Pamir and central Tibet through the Sichuan basin and South China fold system (SCFS) to the Philippine Sea. A pronounced high velocity anomaly is observed beneath entire Tibet down to a depth of 200 km and is interpreted as the

mantle lithosphere. The shallow low-velocity anomaly beneath Tibet is sharply bounded to the east by the mantle lithosphere of the Sichuan basin, seen as high velocity body down to a depth of 175 km. Beneath the Pamir and Hindu Kush high velocity exists down to a depth of 250–300 km. All these anomalies are significant at the 95% confidence level and can be clearly observed in relative and absolute velocity images. From the continental region east of the Sichuan basin to the oceanic area of the Philippine Sea the upper mantle is characterized by low velocity, indicating a thin lithosphere (<100 km). The high velocity beneath Taiwan extends from 100 km depth to at least 300 km. Our long period surface waves cannot resolve a thin slab next to a dominant low velocity mantle wedge. At larger depths low velocity anomalies are weaker, the high-velocity signature of the slab dominates and is picked up by our data. However, it is smeared horizontally by our long period dataset.

Section BB" passes through two cratonic regions (Tarim basin and NCC) and extends to the Tien Shan to the west and to the Philippine Sea to the east. The Tien Shan and the Qilian (QFS) orogenic belt are known to have thick crust whereas the Tarim basin has a normal continental crustal thickness (Li et al., 2006; Zhang et al., 2011). High velocity mantle lithosphere can be clearly seen beneath the Tarim basin in the velocity perturbations as well as in the absolute velocity. In the velocity perturbation image, the high velocity body appears to extend to the west beneath the Tien Shan and to the east beneath the QFS. High velocity mantle lithosphere exists beneath the Ordos block, which constitutes the western part of the NCC. The high velocity lid beneath the eastern NCC is too thin to be observed in our model, and is underlain by low mantle velocities between 75 and 175 km depth. Farther east the subducted oceanic slab of the Philippine Sea and the Pacific plates are associated with high velocity anomalies, in good agreement with the slab seismicity.

In section CC" the low velocity beneath the CAOB centered at the Hangay Dome can be seen as a low velocity anomaly reaching a depth of 100 km at the southern tip of Baikal Lake. Songliao basin in northeast China appears to have a deep lithospheric root as seen in the velocity perturbation, but has no distinct sub-lithospheric low velocity zone. The high velocity signature of the Pacific subducted slab is observed in the mantle beneath Japan and NE China.

The India–Eurasia collision zone can best be examined on section DD", which cuts through the Indian plate, central Tibet, the Hangay Dome and southern Siberia. The most significant feature of our mantle cross-section is the northerly dipping high velocity body, suggesting that the Indian mantle lithosphere underthrusts much of Tibet until the JRS. Beneath the JRS and KF, south of the Qaidam basin, the high velocity mantle layer suddenly jumps to a shallower depth by about 50 km, which we interpret as the start of the Eurasian mantle lithosphere. At either edge of the thick mantle lithosphere beneath the plateau subvertical high velocity bodies are clearly visible at depths between 300 and 400 km, corresponding to the ring of faster velocities seen in map view (Fig. 8, 300 km depth slice).

Section EE" links the Sichuan basin and the Ordos block, which form the western parts of two cratons, the NCC and YC. The lithosphere of both cratons is significantly thicker (>150 km) in the west, while it is much thinner (<70–80 km) in the east (compared to section FF" also see E–W sections AA" and BB"). In the section the Sichuan basin and Ordos block have a different velocity signature. The Sichuan basin is a more pronounced high velocity body, both in perturbation and in absolute velocities, extending to a depth of ~175 km. The Ordos block extends to a depth of ~150 km and is less pronounced in the section of absolute velocity.

Section FF" is located in east China passing through the SCFS, the eastern parts of the YC and the NCC and Songliao basin. The mantle lithosphere beneath the NCC is too thin to be resolved. At very shallow depth (70–80 km) beneath the SCFS and YC high velocities are visible, which we interpret as mantle lithosphere. Beneath Songliao basin high velocities reach a depth of 300 km and spread to the north and

south directions in the depth range of 150–400 km beneath the YC and NCC.

5. Discussions

5.1. Segmentation of lithospheric blocks over China

China consists of Precambrian cratons separated by Phanerozoic fold belts. However, the thickness of the lithosphere does not follow the geographic locations of these tectonic units. It is known from numerous studies (Feng and An, 2010; Feng et al., 2010; Huang et al., 2003; Lebedev and Nolet, 2003; Obrebski et al., 2012; Priestley et al., 2006) that the lithosphere is thin in east China and thick in the west, roughly divided by the North–South Gravity Lineament (NSGL). The NSGL is a major gravity gradient, 100 km wide, which marks the border between west and east China with distinct topographic, tectonic and seismic properties and therefore has been recognized for a long time to be important in the evolution of eastern Asia (Xu, 2007). Across the NSGL, the Bouguer gravity anomaly increases rapidly from -100 mGal in the west to -40 mGal in the east. Our result (Figs. 8–10) confirms the earlier observations but with more detailed information. The depth slice at 100 km in Fig. 8 clearly highlights the mantle lithospheric roots of the cratonic blocks, indicated by high velocities. These include the Tarim basin, west NCC (Ordos block) and west YC (Sichuan basin). The lithospheric roots extend to ~ 150 km depth beneath Ordos block and to ~ 175 km depth beneath Tarim basin and Sichuan basin. These cratonic blocks form the north and east borders of the Indian–Asian collision zone and have acted as rigid blocks resisting the plate motion and guiding lithospheric deformation around them during the collision (see Clark and Royden, 2000; Royden et al., 2008). The northward moving Indian plate has a thickness of 100–175 km with its thickest part in north central India adjacent to Tibet. The seismic lithosphere beneath much of the Pamir–Tibetan plateaus has doubled its thickness during the Indo-Asian collision with a maximum thickness over 200 km beneath the Tibetan plateau.

In the eastern portion of the NCC and YC, the lithosphere is too thin to be well observed by large-scale surface wave studies (Huang et al., 2009; Lebedev and Nolet, 2003; Obrebski et al., 2012; Priestley et al., 2006). We observe a weak high velocity signature which may mark the bottom of the high velocity mantle lithosphere beneath the east YC, but are still missing that of the NCC. Fig. 9 (cross section FF'') suggests that the lithosphere of the east YC is 70–80 km thick, while the lithosphere of the east NCC would be thinner than ~ 70 km and therefore not resolved by our data. A thin lithosphere beneath the cratonic areas in east China is supported by receiver function studies. The base of the lithosphere beneath the east NCC was estimated by receiver functions as shallow as ~ 60 km, whereas it is ~ 10 km deeper in the east YC (Chen, 2009; Chen et al., 2008; Sodoudi et al., 2006). However, although our test (Figs. S3–S5) suggests that our data pick up high velocities of a shallow mantle lithosphere in east China, it is important to keep in mind that this high velocity signature is only constrained locally at the 68% confidence level, and that shallow structure down to about 100 km depth may trade-off with crustal structure, an effect which is not accounted for in our tests.

5.2. Sub-lithospheric structure

The subducted Pacific slab has been clearly imaged by body wave tomography (e.g., Huang and Zhao, 2006; Li et al., 2008). In some places,

we pick up the signature of a high velocity oceanic slab with surface waves, but the lateral resolution is not as good as that of body waves. In the northwest Pacific subduction zones the subducted oceanic lithosphere can be followed to a depth of 200–300 km (Figs. 8 and 9). The wide-spread low velocity anomalies following plate boundaries at shallower depths (< 100 km) are likely to represent mantle wedges. In the depth range of 100–300 km we can recognize the downgoing slab by high velocities. At larger depths (greater than 300 km) the resolution is insufficient to clearly image the slab. A pronounced high velocity body is resolved at the 95% confidence level beneath Taiwan at a depth range of 150–300 km. High velocity anomalies have also been observed by body wave tomography (Huang et al., 2010) and surface wave tomography (Sibuet et al., 2004) and were interpreted as evidence for a subducted Eurasian slab beneath Taiwan. Ai et al. (2007) observed a thickening in the mantle transition zone beneath Taiwan, which is compatible with the high velocity Ryukyu slab penetrating the mantle transition zone.

No high velocity mantle lithosphere is recognized along the CAOB that extends from the Altai Mountains to the east to the Pacific Ocean. Widespread low velocity anomalies exist below the crust to a depth of 300 km (Figs. 8 and 9 sections C–E). Kustowski et al. (2008) also observed a low velocity upper mantle below the CAOB. The most prominent low velocity anomaly is located beneath the Hangay Dome and is visible down to a depth of 150 km, as also observed by Priestley et al. (2006).

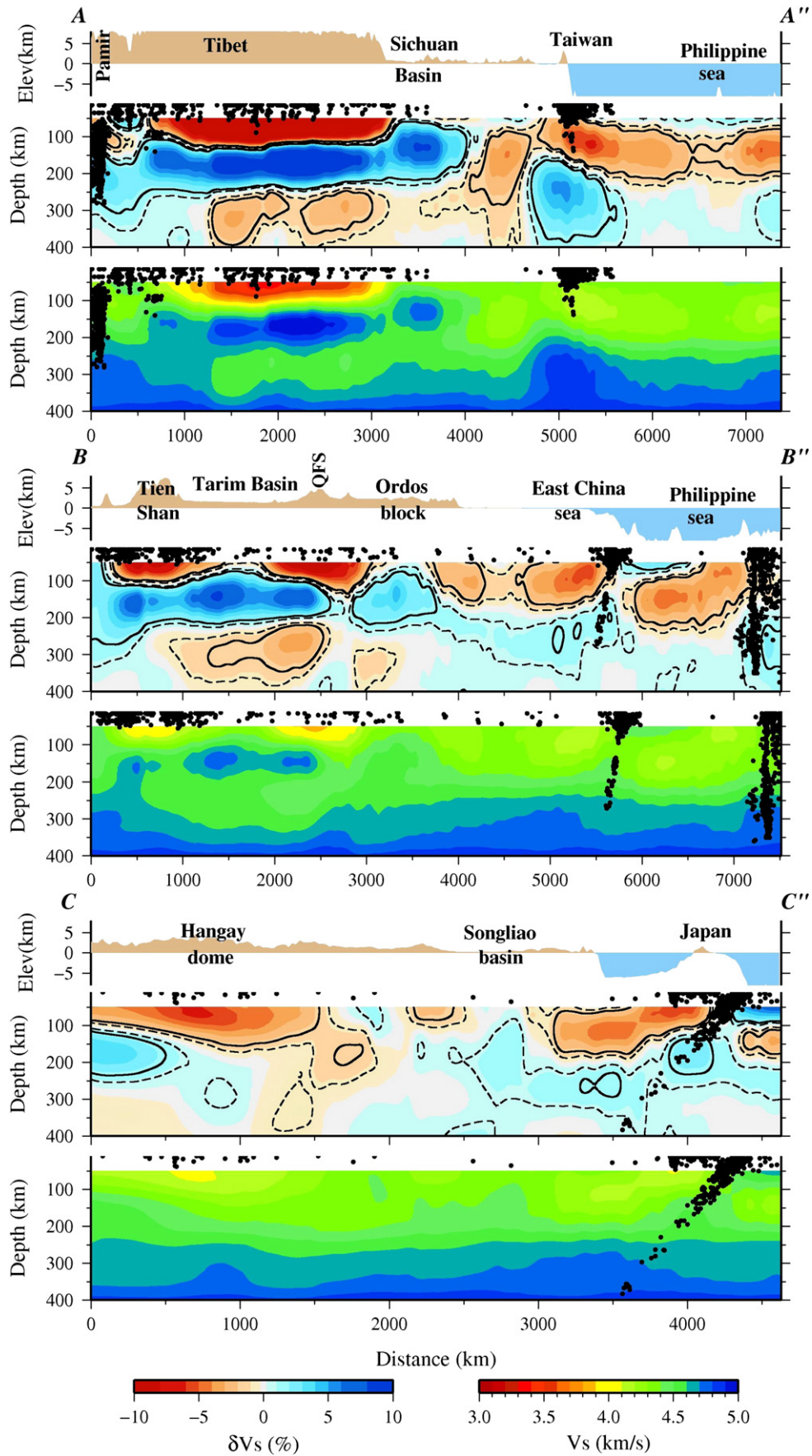
In the Songliao basin, northeast China, there is no significant low velocity zone in the sub-lithospheric mantle. Instead, a weak high velocity anomaly is constrained at the 68% confidence level from about 100 km depth to a depth of 300 km and connects in the depth range of 150–350 km to a large-scale subhorizontal high velocity body that spreads from below the Songliao basin ~ 500 km to the north and more than 2000 km to the south underlying the entire YC and NCC (Figs. 8 and 9, sections CC'' and FF''). In the next section we interpret this large-scale high velocity body, which is constrained with a confidence level greater than 68%, as delaminated mantle lithosphere underlying the entire cratonic area beneath east China.

5.3. Destruction of the lithosphere beneath the east China cratonic areas

The eastern portion of mainland China comprises different tectonic units, including two major cratons (NCC and YC), Songliao basin and Xing'an Ranges north of NCC and the South China Fold System (SCFS) south of YC (see Fig. 1). A common feature of the entire region is that the lithosphere is thin. The NS trending NSGL marks a sharp transition of the thickness of the lithosphere from east to west. We observed the base of the high velocity mantle lid beneath the YC and SCFS at ~ 80 km depth. Low velocities beneath the NCC indicate a thinner lithosphere there. Beneath the Songliao basin, although we did not observe a significant low velocity zone in the sub-lithospheric mantle, Sun et al. (2010) and Zheng et al. (2011) showed with ambient noise tomography that the lithosphere is ~ 70 km thick in the area. We have seen that trade-offs with crustal structure may bias our estimation of the shear wave velocity in the uppermost 100 km, so that resolving a seismic lithosphere thinner than 70 km with our approach is difficult.

The NCC and YC are two ancient cratons, which have formed and consolidated during Paleoproterozoic time and collided during Triassic time (Yang et al., 2010; Zhu et al., 2012). Diamond-bearing kimberlites erupted at ~ 470 Ma provide evidence of a thick (> 200 km) lithosphere

Fig. 9. Cross-sections of Sv velocity perturbation and absolute velocity along 3 EW lines A–C and 3 NS lines D–F. Locations of the profiles are indicated in Fig. 8. Color scales for relative and absolute velocities are indicated at the bottom. Surface topography is plotted on top of each profile with major tectonic units indicated. Black dots denote the relocated earthquakes from the EHB catalog (Engdahl and van der Hilst, 1998) within 100 km in either side of the profile. Contour lines surround the areas whose anomalies (i.e. deviations from the reference model) are significant at least at the 68% (dashed lines) and 95% (solid lines) confidence levels. Abbreviations: QFS, Qilian fold system; CAOB, Central Asia Orogenic Belt; SCFS, South China fold system; YC, Yangtze craton; NCC, North China craton.



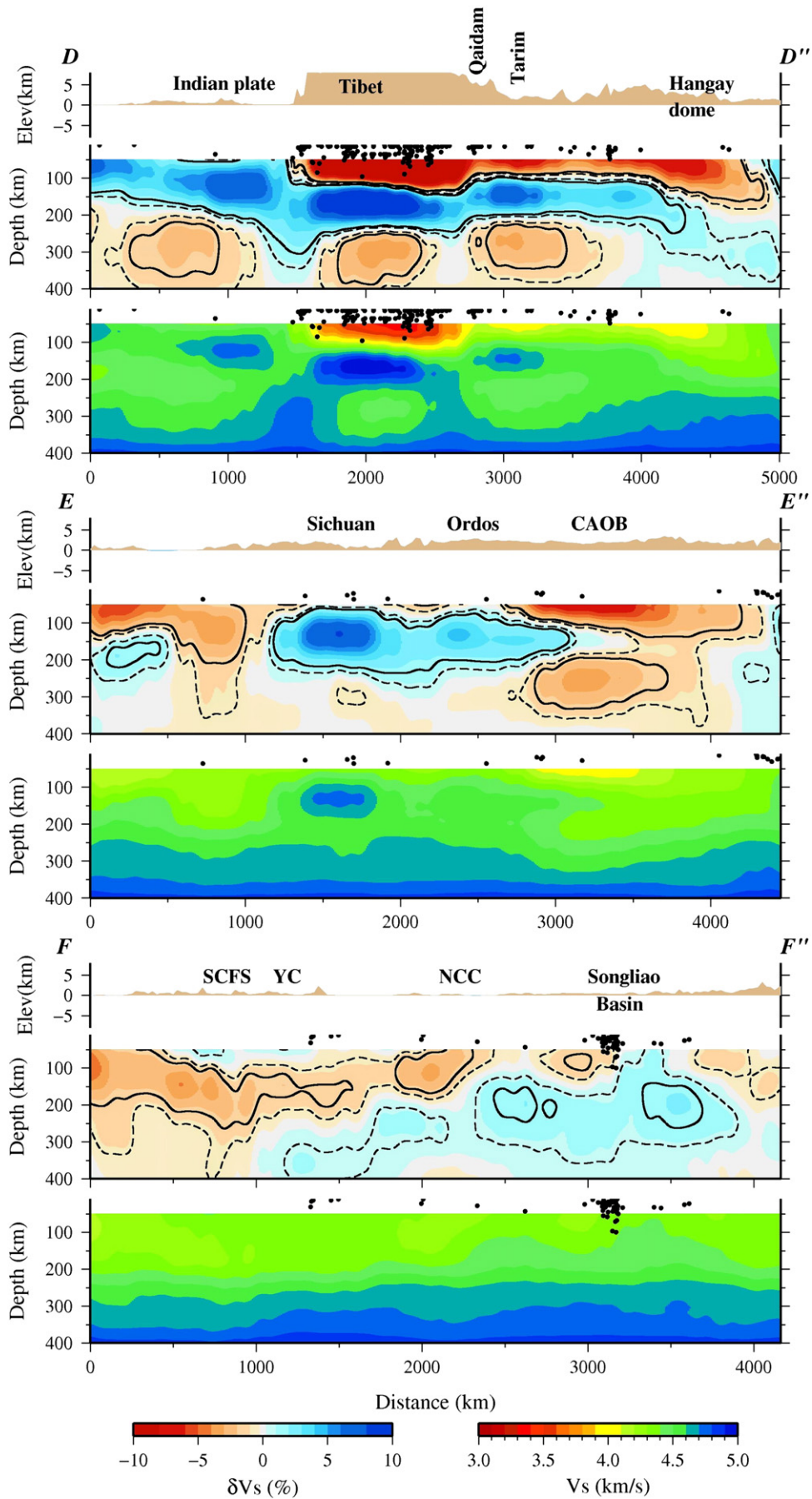


Fig. 9 (continued).

at that time. However, the Cenozoic basalts sampled a thin lithosphere of 80–120 km thickness (e.g., Griffin et al., 1998; Kusky et al., 2007; Menzies and Xu, 1998; Yang et al., 2010; Zhu et al., 2012). Therefore, it is commonly agreed that the thick lithosphere beneath the ancient cratons of the NCC and YC has been destroyed in the Mesozoic and the depleted cratonic lithospheric root has been removed. However, the extent and mechanism of the destruction of the lithospheric keel are an open debate (see Zhu et al., 2012, for a review). The region is characterized by high heat flow and extensive seismicity (Ma et al., 1984; Wesnousky et al., 1984). The extension experienced since the Mesozoic, together with Cenozoic volcanism in this area (Menzies and Xu, 1998; Yang et al., 2010), caused by delamination or thermal erosion of the thick lithospheric root (Kusky et al., 2007), may be responsible for the lithospheric thinning. Different tectonic events proposed to be responsible for the decratonization of the NCC and YC include the India–Eurasia collision, the mantle plume activity, the collision of these two cratons and the west Pacific plate subduction. Recent studies tend to agree that the latter is the major trigger for the decratonization (reviewed by Zhu et al., 2012).

We observed widespread high velocities, constrained with a confidence level greater than 68%, at 150 to 350 km depth underlying the whole area of Songliao basin and the eastern portion of the North China and Yangtze Cratons (Fig. 9, CC' and FF'). Priestley et al. (2006) reported on observation of a high-velocity feature beneath Songliao basin. Obrebski et al. (2012) also observed a fast anomaly at 200 km depth beneath the NCC and interpreted it as a possible delaminated lithospheric root of the NCC. Our result confirms their observation but we show that the high velocity anomalies are distributed over a much larger area, 100–200 km in thickness and ~3000 km in length. Up to three local maxima (underneath the YC, NCC and Songliao basin) can be discerned in the wider high velocity anomaly, and it is possible that smearing makes more localized anomalies under these three regions appear connected. The high velocity zone in our mantle model is parallel to the Pacific subduction zone, underlies the entire region of the eastern China cratons, and is bordered to the west by the NSGL. It is still unclear how and when the NSGL formed, or whether it is even related to the lithospheric deformation. However, the NSGL marks the western border of the sub-lithospheric high velocity zone along its ~3000 km length in our model.

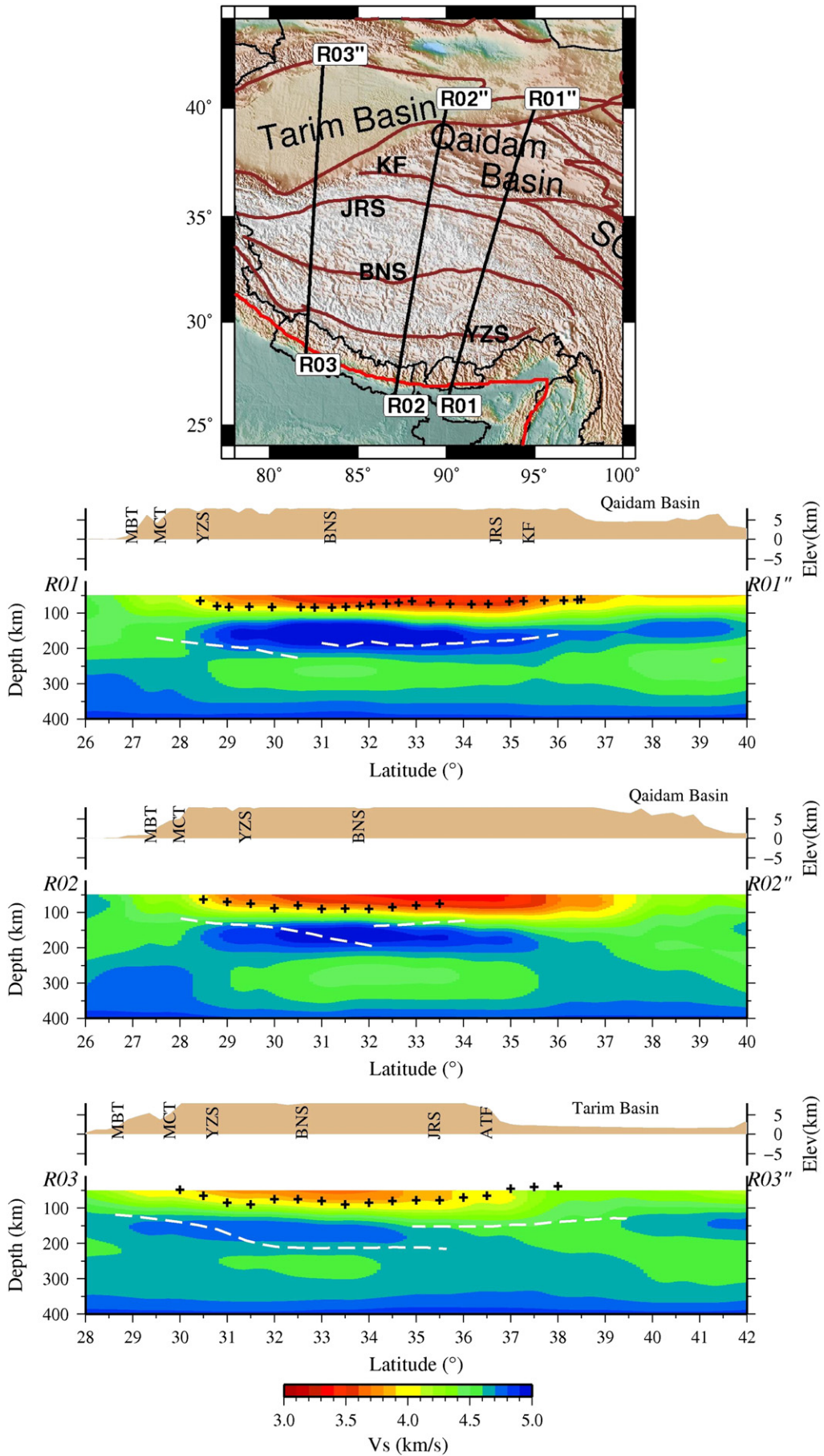
Various studies have shown that the eastern portion of the North China Craton does not possess a lithospheric root similar to those commonly seen beneath almost all other cratons (Kusky et al., 2007; Menzies and Xu, 1998; Zhu et al., 2012). The timing of root loss is not well constrained but seems to be ca. 140–120 Ma (Kusky et al., 2007). Two main scenarios proposed in previous studies are density foundering or delamination (Gao et al., 2004; Kusky et al., 2007; Windley et al., 2010; Xu et al., 2013) and thermal–chemical erosion (Menzies and Xu, 1998). Recycled continental crust has been found in the NCC, suggesting that the lower part of cratonic mantle lithosphere has delaminated since the Mesozoic (Gao et al., 2004; Xu et al., 2013). Delamination is a sudden process that seems to agree with the timing of the lithospheric root loss of the NCC, however, a simultaneous response of the entire cratonic areas to this catastrophic loss is not yet clear (Kusky et al., 2007). Among different mechanisms, the decratonization of the North China Cratons is very likely related to the Mesozoic Pacific subduction beneath eastern China (Xu, 2007; Zhu et al., 2012). This hypothesis is supported by our observation that the large-scale high velocity body in sub-lithospheric mantle is parallel to the NSGL and the Pacific subduction zone. This high velocity anomaly may represent a remnant lithospheric root, which initially formed the lower part of cratonic mantle lithosphere and has delaminated since the Mesozoic. If this is the case, it is not clear how buoyant, depleted lower lithosphere can flounder nor is it clear how the delaminated material can persist in the upper mantle for such a long time duration. It is surprising that lithospheric material from a delamination event in the Mesozoic still remains in the upper mantle.

Maybe the underlying subducted oceanic slab prevents its further descent. Subducted oceanic slab has been found to stagnate in the mantle transition zone below east China (e.g., Huang and Zhao, 2006; Li et al., 2008), providing a possible barrier for the delaminated lithospheric block from sinking deeper into the mantle. In fact, parts of the delaminated body might have contacted and joined the subducted oceanic slab. Although our observation favors the delamination model, the fundamental debates between delamination and erosion still remain.

5.4. The India–Asia collision zones

We observe a thick high velocity mantle lid underlying much of the Tibetan plateau (Figs. 8, 9). High velocity underthrust Indian plate has also been observed by global body wave tomography (e.g., Li et al., 2008), but with this technique seen to be limited to the southern Tibetan plateau (see also Kind and Yuan, 2010). Regional body wave tomography may reveal more lateral variation in the mantle lithosphere (e.g., Liang et al., 2012), but is less sensitive to a subhorizontal lithosphere with a large lateral extent. Most surface wave studies observed high mantle velocities over much of the plateau (e.g., Huang et al., 2003; Lebedev and Nolet, 2003; Priestley et al., 2006, 2008a). This discrepancy can be largely explained by different resolutions of the body wave and surface wave studies (Nunn et al., 2014). However, the surface wave studies of Friederich (2003) as well as Feng and An (2010) and Feng et al. (2010) infer a low velocity zone in the upper 200 km beneath north Tibet. Agius and Lebedev (2013) infer low velocities to ~150 km depth in northern Tibet from two-station dispersion measurements, with high velocities at larger depths, an observation which can partially reconcile with both set of apparently contrasting surface wave observations. Observations of Pn (Hearn et al., 2004; Liang and Song, 2006; McNamara et al., 1997) and Sn propagation (Barazangi and Ni, 1982; Barron and Priestley, 2009; McNamara et al., 1995) point to low velocities and high attenuation immediately below the Moho north of the BNS. This might correspond to the localized low velocity zone we observe along the JRS and KF south of Tarim and Qaidam basins (see map at 125 km depth in Fig. 8) and also to the shallow northward dip of the top of the high velocity layer visible in cross-section D–D' (Fig. 9). Using surface waves recorded by temporary experiments within Tibet, Ceylan et al. (2012) observed high velocity, probably Indian plate underthrusting Tibet up to about 34°N, coincident with the JRS in Eastern Tibet. Supporting evidence for a less attenuative and probably higher velocity mantle at depths of more than ~130 km comes from the frequency dependence of Sn attenuation in Northern Tibet (Barron and Priestley, 2009). Ceylan et al. (2012) additionally revealed a very localized deep-seated low velocity zone below and just north of the Kunlun Mountains, extending in depth to the limit of their resolution (~220 km). The body wave tomography images of Liang et al. (2012) also show this low-velocity feature whose N–S width is only around 200 km and is therefore not reliably imaged by our surface wave tomography. However, we did not observe a large-scale low velocity mantle zone in north Tibet that could represent a major upwelling of asthenosphere. Instead, the localized mantle low velocity zone probably marks the northern border of either underthrust India or the overthickened Tibetan lithosphere, separating the Tibetan plateau from the Tarim basin and Tien Shan. As the properties of Indian and Tibetan mantle lithosphere might be quite similar, it is not possible to distinguish between these alternatives using seismological data.

In Fig. 10 we compare the surface wave models with those obtained by P- and S-receiver functions (Zhao et al., 2010). Along all the sections we marked the positions of the Moho and LAB observed by Zhao et al. (2010) on the absolute velocity profiles derived by the surface wave inversion (Fig. 10). Below the crust the high velocity mantle lithosphere often finds agreement with the line drawings of the receiver function LAB. This is the case for the Indian LAB, represented by the



white dashed lines in the southern part of the sections. The Asian LAB, which is observed from S-receiver functions and is indicated by the dashed lines in the central and northern part of the sections, is only matching the base of the high velocity body on the east line (R01), but is not seen by the surface waves on the central (R02) and west lines (R03). The lower lateral resolution might prevent surface waves from observing the fine structure seen by receiver functions, which are more sensitive to the interior structure of incipient fragmentation of the Indian slab below Tibet (see Ceylan et al., 2012; Liang et al., 2012). It is also possible that receiver functions do not see the base of the lithosphere, but a mid-lithospheric structure, as reported for the North American craton (Abt et al., 2010; Kumar et al., 2012).

6. Conclusion

We derived 3-D upper mantle absolute shear wave velocities by modeling fundamental and higher mode waveforms of surface waves. We extended the multi-mode surface tomography of East Asia of Priestley et al. (2006) by adding more permanent stations within China and constrained the study area to China and its close vicinity. The reduced inter-station distances enabled us to reduce the lateral smoothing by using a smaller Gaussian correlation length during the regionalization approach, thus increasing lateral resolution. We created a 3D S velocity model over China with a good resolution from the top of the upper mantle to a depth of ~400 km. Compared to earlier studies, velocity anomalies are better and more sharply defined in the model. Similar to Priestley et al. (2006) the velocity perturbation decreases from ~10% at shallow depths to ~2% at depths of 300–400 km. Although synthetic recovery tests indicate that magnitude of anomalies below 200 km is not fully recovered, the reduction in percentage anomaly is too large to be explained by the reduced resolution alone. At 100–200 km depth the model is sensitive to the lateral variation of the thickness of the mantle lithosphere. The seismic lithosphere is generally thinner in east China and thick in West China. It reaches a thickness of 200 km beneath the Pamir–Tibetan plateaus. Also observed as relatively thick seismic lithosphere (> 100 km) are the Indian plate, Sichuan basin, Ordos block and Tarim basin. The lithosphere in the eastern part of the Yangtze craton is as thin as 70–80 km, whereas the lithosphere of the North China craton is too thin to be resolved. Beneath these two cratons, an extensive high velocity body at depths of 150–350 km is observed and resolved with a confidence level greater than 68%. A possible interpretation is to associate this body with the remnant ancient lithospheric material from a large scale delamination event that was proposed to be the cause of the decratonization of Eastern China. This suggestion needs to be probed in future studies, though.

Acknowledgments

The work is funded by the Deutsche Forschungsgemeinschaft (grant number YU 115/2). Waveform data were downloaded from the Chinese Earthquake Network Center, the IRIS and the GEOFON data centers. We also thank the operators of the many temporary and permanent networks used. We appreciate Marcelo Bianchi and James Mechie for their help with computational aspects. We thank two anonymous reviewers and the editor Hans Thybo for comments, improving the clarity of the manuscript and pushing us to provide a more quantitative assessment of uncertainty. We also thank two anonymous reviewers of an earlier version of this manuscript.

References

- Abt, D.L., Fischer, K.M., French, S.W., Ford, H.A., Yuan, H.Y., Romanowicz, B., 2010. North American lithospheric discontinuity structure imaged by PS and SP receiver functions. *J. Geophys. Res.* 115, B09301. <http://dx.doi.org/10.1029/2009JB006914>.
- Agius, M.R., Lebedev, S., 2013. Tibetan and Indian lithospheres in the upper mantle beneath Tibet: evidence from broadband surface-wave dispersion. *Geochem. Geophys. Geosyst.* 14 (10), 4260–4281. <http://dx.doi.org/10.1002/ggge.20274>.
- Ai, Y.S., Chen, Q.F., Zeng, F., Hong, X., Ye, W.Y., 2007. The crust and upper mantle structure beneath southeastern China. *Earth Planet. Sci. Lett.* 260, 549–563.
- Anderson, D.L., 1995. Lithosphere, asthenosphere, and perisphere. *Rev. Geophys.* 33, 125–149.
- Barazangi, M., Ni, J., 1982. Velocities and propagation characteristics of Pn and Sn beneath the Himalayan arc and Tibetan Plateau: possible evidence for underthrusting of Indian continental lithosphere beneath Tibet. *Geology* 10, 179–185.
- Barrell, J., 1914. The strength of the Earth's crust. *J. Geol.* 22, 655–683.
- Barron, J., Priestley, K., 2009. Observations of frequency-dependent Sn propagation in Northern Tibet. *Geophys. J. Int.* 179, 475–488. <http://dx.doi.org/10.1111/j.1365-246X.2009.04318.x>.
- Cara, M., L  v  que, J., 1987. Waveform inversion using secondary observables. *Geophys. Res. Lett.* 14, 1046–1049.
- Ceylan, S., Ni, J., Chen, J.Y., Zhang, Q., Tilmann, F., Sandvol, E., 2012. Fragmented Indian plate and vertically coherent deformation beneath eastern Tibet. *J. Geophys. Res.* 117, B11303. <http://dx.doi.org/10.1029/2012JB009210>.
- Chen, L., 2009. Lithospheric structure variations between the eastern and central North China Craton from S- and P-receiver function migration. *Phys. Earth Planet. Inter.* 173, 216–227.
- Chen, L., Tao, W., Zhao, L., Zheng, T.Y., 2008. Distinct lateral variation of lithospheric thickness in the northeastern North China Craton. *Earth Planet. Sci. Lett.* 267, 56–68.
- Clark, M.K., Royden, L.-H., 2000. Topographic ooze: building the eastern margin of Tibet by lower crustal flow. *Geology* 28, 703–706.
- Curtis, A., Trampert, J., Snieder, R., Dost, B., 1998. Eurasian fundamental mode surface wave phase velocities and their relationship with tectonic structures. *J. Geophys. Res.* 103, 26,919–26,947.
- Debayle, E., 1999. Sv-wave azimuthal anisotropy in the Australian upper mantle: preliminary results from automated Rayleigh waveform inversion. *Geophys. J. Int.* 137, 747–754.
- Debayle, E., Kennett, B.L.N., 2000. The Australian continental upper mantle: structure and deformation inferred from surface waves. *J. Geophys. Res.* 105, 25423–25450.
- Debayle, E., L  v  que, J.-J., 1997. Upper mantle heterogeneities in the Indian Ocean from waveform inversion. *Geophys. Res. Lett.* 24, 245–248.
- Debayle, E., Ricard, Y., 2012. A global shear velocity of the upper mantle from fundamental and higher Rayleigh mode measurements. *J. Geophys. Res.* 117, B10308. <http://dx.doi.org/10.1029/2012JB009288>.
- Debayle, E., Sambridge, M., 2004. Inversion of massive surface wave data sets: model construction and resolution assessment. *J. Geophys. Res.* 109, B02316. <http://dx.doi.org/10.1029/2003JB002652>.
- Debayle, E., L  v  que, J.-J., Cara, M., 2001. Seismic evidence for a deeply rooted low velocity anomaly in the upper mantle beneath the northeastern Afro/Arabian continent. *Earth Planet. Sci. Lett.* 193, 423–436.
- Eaton, D.W., Darbyshire, F., Evans, R.L., Gr  tter, H., Jones, A.G., Yuan, X., 2009. The elusive lithosphere–asthenosphere boundary (LAB) beneath cratons. *Lithos* 109, 1–22.
- Engdahl, E.R., van der Hilst, R., 1998. Global teleseismic earthquake relocation with improved travel times and procedures for depth determination. *Bull. Seismol. Soc. Am.* 88, 722–743.
- Feng, M., An, M., 2010. Lithospheric structure of the Chinese mainland determined from joint inversion of regional and teleseismic Rayleigh wave group velocities. *J. Geophys. Res.* 115, B06317. <http://dx.doi.org/10.1029/2008JB005787>.
- Feng, M., van der Lee, S., An, M., Zhao, Y., 2010. Lithospheric thickness, thinning, subduction, and interaction with the asthenosphere beneath China from the joint inversion of seismic S-wave train fits and Rayleigh-wave dispersion curves. *Lithos* 120, 116–130.
- Friederich, W., 2003. The S-velocity structure of the East Asian mantle from inversion of shear and surface waveforms. *Geophys. J. Int.* 153, 88–102.
- Gao, S., Rudnick, R.L., Yuan, H.L., Liu, X., Liu, Y.S., Xu, W.L., Ling, W.L., Ayers, J., Wang, X.C., Wang, Q.H., 2004. Recycling lower continental crust in the North China craton. *Nature* 432, 892–897.
- Griffin, W.L., Andi, Z., O'Reilly, S.Y., Ryan, C.G., 1998. Phanerozoic evolution of the lithosphere beneath the Sino-Korean Craton. In: Flower, M.F.L., Chung, S.L., Lo, C.H., Lee, T.Y. (Eds.), *Mantle Dynamics and Plate Interaction in East Asia*. *Geodyn. Ser.*, vol. 27. AGU, Washington D.C., pp. 107–126.
- Griot, D., Montagner, J., Tapponnier, P., 1998. Phase velocity structure from Rayleigh and Love waves in Tibet and its neighboring regions. *J. Geophys. Res.* 103, 21,215–21,232.
- Hearn, T.M., Wang, S., Ni, J.F., Xu, Z., Yu, Y., Zhang, X., 2004. Uppermost mantle velocities beneath China and surrounding regions. *J. Geophys. Res.* 109, B11301. <http://dx.doi.org/10.1029/2003JB002874>.
- Heintz, M., Debayle, E., Vauchez, A., 2005. Upper mantle structure of the South American continent and neighboring oceans from surface wave tomography. *Tectonophysics* 406, 115–139.

Fig. 10. Comparison of the upper mantle model with three receiver function profiles in Tibet (Zhao et al., 2010). Along each profile, the upper panel shows the topography and the lower panel shows the upper mantle absolute velocities along the profile. Locations of the Moho and the LAB, derived by Zhao et al. (2010) from P- and S-receiver functions, respectively are indicated in the velocity profiles.

- Huang, J., Zhao, D., 2006. High-resolution mantle tomography of China and surrounding regions. *J. Geophys. Res.* 111, B09305. <http://dx.doi.org/10.1029/2005JB004066>.
- Huang, T.K., Jen, C., Jiang, C., Chang, Z., Chin, D., 1980. *The Geotectonic Evolution of China*. Academic Publishing House, Beijing, China, p. 124.
- Huang, Z., Su, W., Peng, Y., Zheng, Y., Li, H., 2003. Rayleigh wave tomography of China and adjacent regions. *J. Geophys. Res.* 108, 2073. <http://dx.doi.org/10.1029/2001JB001696>.
- Huang, Z., Li, H., Zheng, Y., Peng, Y., 2009. The lithosphere of North China Craton from surface wave tomography. *Earth Planet. Sci. Lett.* 288, 164–173.
- Huang, Z., Wang, L., Zhao, D., Xu, M., Mi, N., Yu, D., Li, H., Li, C., 2010. Upper mantle structure and dynamics beneath Southeast China. *Phys. Earth Planet. Inter.* 182, 161–169.
- Kennett, B.L.N., 1995. Approximations for surface-wave propagation in laterally varying media. *Geophys. J. Int.* 122, 470–478.
- Kind, R., Yuan, X., 2010. Seismic images of the biggest crash on earth. *Science* 329, 1479–1480.
- Kind, R., Yuan, X., Saul, J., Nelson, D., Sobolev, S.V., Mechie, J., Zhao, W., Kosarev, G., Ni, J., Achauer, U., Jiang, M., 2002. Seismic images of crust and upper mantle beneath Tibet: evidence for Eurasian plate subduction. *Science* 298, 1219–1221.
- Kumar, P., Kind, R., Yuan, X., Mechie, J., 2012. USArray receiver function images of the LAB. *Seismol. Res. Lett.* 83, 486–491.
- Kusky, T.M., Windley, B.F., Zhai, M., 2007. Lithospheric thinning in eastern Asia: constraints, evolution, and tests of models. In: Zhai, M., Windley, B.F., Kusky, T.M., Meng, Q. (Eds.), *Mesozoic sub-continental lithospheric thinning under Eastern Asia*. Geological Society, London, Special Publications, 280, pp. 331–343.
- Kustowski, B., Ekström, G., Dziewonski, A.M., 2008. The shear-wave velocity structure in the upper mantle beneath Eurasia. *Geophys. J. Int.* 174, 978–992.
- Lebedev, S., Nolet, G., 2003. Upper mantle beneath Southeast Asia from S velocity tomography. *J. Geophys. Res.* 108, 2048. <http://dx.doi.org/10.1029/2000JB000073>.
- Lévéque, J.J., Rivera, L., Wittlinger, G., 1993. On the use of the checker-board test to assess the resolution of tomographic inversions. *Geophys. J. Int.* 115, 313–318.
- Li, S., Mooney, W.D., Fan, J., 2006. Crustal structure of mainland China from deep seismic sounding data. *Tectonophysics* 420, 239–252.
- Li, C., van der Hilst, R.D., Meltzer, A.S., Engdahl, E.R., 2008. Subduction of the Indian lithosphere beneath the Tibetan Plateau and Burma. *Earth Planet. Sci. Lett.* 274, 157–168.
- Liang, C., Song, X., 2006. A low velocity belt beneath northern and eastern Tibetan Plateau from Pn tomography. *Geophys. Res. Lett.* 33, L22306. <http://dx.doi.org/10.1029/2006GL027926>.
- Liang, X., Sandvol, E., Chen, Y.J., Hearn, T., Ni, J., Klempner, S., Shen, Y., Tilmann, F., 2012. A complex Tibetan upper mantle: a fragmented Indian slab and no south-verging subduction of Eurasian lithosphere. *Earth Planet. Sci. Lett.* 333–334, 101–111.
- Liu, M., Yang, Y., Shen, Z.K., Wang, S., Wang, M., Wan, Y., 2007. Active tectonics and intracontinental earthquakes in China: the kinematics and geodynamics. In: Stein, S., Mazzotti, S. (Eds.), *Continental intraplate earthquakes: science, hazard, and policy issues*. Geological Society of America Special Paper, 425. Geological Society of America, Boulder, CO, pp. 299–318.
- Ma, X.-Y., 1987. *Summary of Lithospheric Dynamics in China*. Geological Press, Beijing.
- Ma, X., Liu, G., Su, J., 1984. The structure and dynamics of the continental lithosphere in north-northeast China. *Ann. Geophys.* 2, 611–620.
- McNamara, D., Owens, T., Walter, W., 1995. Observation of regional propagation across the Tibetan Plateau. *J. Geophys. Res.* 100, 22,215–22,229.
- McNamara, D., Walter, W., Owens, T., Ammon, C., 1997. Upper mantle velocity structure beneath the Tibetan Plateau from Pn travel time tomography. *J. Geophys. Res.* 102, 493–505.
- Menzies, M.A., Xu, Y., 1998. Geodynamics of the North China Craton. In: Flower, M.F.L., Chung, S.L., Lo, C.H., Lee, T.Y. (Eds.), *Mantle dynamics and plate interactions in East Asia*. Geodynamics Series, vol. 27. AGU, Washington, DC, pp. 155–165.
- Montagner, J., 1986. Regional three-dimensional structures using long-period surface waves. *Ann. Geophys.* 4, 283–294.
- Nataf, H.C., Ricard, Y., 1995. 3SMAC: an a priori tomographic model of the upper mantle based on geophysical modeling. *Phys. Earth Planet. Inter.* 1–2, 101–122.
- Nishimura, C.E., Forsyth, D.W., 1989. The anisotropic structure of the upper mantle in the Pacific. *Geophys. J. Int.* 96, 203–229.
- Nunn, C., Roecker, S.W., Tilmann, F., Priestley, K.F., Heyburn, R., Sandvol, E.A., Ni, J.F., Chen, Y. J., Zhao, W., INDEPTH IV Team, 2014. Imaging the lithosphere beneath NE Tibet: teleseismic P and S body wave tomography incorporating surface wave starting models. *Geophys. J. Int.* 196 (3), 1724–1741. <http://dx.doi.org/10.1093/gji/ggt476>.
- Obrebski, M., Allen, R.M., Zhang, F., Pan, J., Wu, Q., Hung, S.H., 2012. Shear wave tomography of China using joint inversion of body and surface wave constraints. *J. Geophys. Res.* 117, B01311. <http://dx.doi.org/10.1029/2011JB008349>.
- Pilidou, S., Priestley, K., Gudmundsson, G., Debayle, E., 2004. Upper mantle S-wavespeed heterogeneity beneath the North Atlantic from regional surface waveform tomography: high resolution image of the Iceland plume. *Geophys. J. Int.* 159, 1057–1076.
- Priestley, K., Tilmann, F., 2009. Relationship between the upper mantle high velocity seismic lid and the continental lithosphere. *Lithos* 109, 112–124.
- Priestley, K., Debayle, E., McKenzie, D., Pilidou, S., 2006. Upper mantle structure of eastern Asia from multi-mode surface waveform tomography. *J. Geophys. Res.* 111, B10304. <http://dx.doi.org/10.1029/2005JB004082>.
- Priestley, K., Jackson, J., McKenzie, D., 2008a. Lithospheric structure and deep earthquakes beneath India, the Himalaya and southern Tibet. *Geophys. J. Int.* 172, 345–362. <http://dx.doi.org/10.1111/j.1365-246X.2007.03636.x>.
- Priestley, K., McKenzie, D., Debayle, E., Pilidou, S., 2008b. The African upper mantle and its relationship to tectonics and surface geology. *Geophys. J. Int.* 175, 1108–1126.
- Ritzwoller, M.H., Levshin, A.L., 1998. Eurasian surface wave tomography: group velocities. *J. Geophys. Res.* 103, 4839–4878.
- Romanowicz, B.A., 1982. Constraints on the structure of the Tibet Plateau from pure path phase velocities of Love and Rayleigh waves. *J. Geophys. Res.* 87, 6865–6883.
- Royden, L.H., Burchfiel, B.C., van der Hilst, R.D., 2008. The geological evolution of the Tibetan plateau. *Science* 321, 1054–1058.
- Sibuet, J.C., Hsu, S.K., Debayle, E., 2004. Continent–ocean interactions within the East Asian Marginal Seas. In: Cliff, P. (Ed.), *Geodynamic context of the Taiwan orogen*. AGU Geophysical Monograph Series, 149, pp. 127–158. <http://dx.doi.org/10.1029/149GM08>.
- Sieminski, A., Lévêque, J.J., Debayle, E., 2004. Can finite-frequency effects be accounted for in ray theory surface wave tomography? *Geophys. Res. Lett.* 31, L24614. <http://dx.doi.org/10.1029/2004GL021402>.
- Soudou, F., Yuan, X., Liu, Q., Kind, R., Chen, J., 2006. Lithospheric thickness beneath the Dabie Shan, central eastern China from S receiver functions. *Geophys. J. Int.* 166, 1363–1367.
- Sun, X., Song, X., Zheng, S., Yang, Y., Ritzwoller, M.H., 2010. Three dimensional shear wave velocity structure of the crust and upper mantle beneath China from ambient noise surface wave tomography. *Earthq. Sci.* 23, 449–463.
- Takeuchi, H., Saito, M., 1972. Seismic surface waves. In: Bolt, B.A. (Ed.), *35 Seismology: surface waves and earth oscillations*. Methods in Computational Physics, vol. 11. Academic Press, San Diego, Calif., pp. 217–295.
- Tarantola, A., Valette, B., 1982. Generalized nonlinear inverse problems solved using the least squares criterion. *Rev. Geophys.* 20, 219.
- Trampert, J., Woodhouse, J.H., 1995. Global phase velocity maps of Love and Rayleigh waves between 40 and 150 seconds. *Geophys. J. Int.* 122, 675–690.
- Wesnousky, S., Jones, L., Scholz, C., Adams, D.Q., 1984. Historical seismicity and rates of crustal deformation along the margins of the Ordos block, north China. *Bull. Seismol. Soc. Am.* 74, 1767–1783.
- Windley, B.F., Alexeiev, D., Xiao, W., Kröner, A., Badarch, G., 2007. Tectonic models for accretion of the Central Asian orogenic belt. *J. Geol. Soc. Lond.* 164, 31–47.
- Windley, B.F., Maruyama, S., Xiao, W.J., 2010. Delamination/thinning of subcontinental lithospheric mantle under eastern China: the role of water and multiple subduction. *American Journal of Science* 310, 1250–1293.
- Woodhouse, J., Jun, H., 1974. Surface waves in a laterally varying layered structure. *Geophys. J. Int.* 37, 461–490.
- Xu, Y.-G., 2007. Diachronous lithospheric thinning of the North China Craton and formation of the Daxin'anling–Taihangshan gravity lineament. *Lithos* 96, 281–298.
- Xu, W.-L., Zhou, Q.-J., Pei, F.-P., Yang, D.-B., Gao, S., Li, Q.-L., Yang, Y.-H., 2013. Destruction of the North China Craton: delamination or thermal/chemical erosion? Mineral chemistry and oxygen isotope insights from websterite xenoliths. *Gondwana Res.* 23, 119–129.
- Yang, J.-H., O'Reilly, S., Walker, R.J., Griffin, W., Wu, F.-Y., Zhang, J., Pearson, N., 2010. Diachronous decratonization of the Sino-Korean craton: geochemistry of mantle xenoliths from North Korea. *Geology* 38, 799–802.
- Yin, A., Harrison, T.M., 2000. Geologic evolution of the Himalayan–Tibetan orogen. *Annu. Rev. Earth Planet. Sci.* 28, 211–280.
- Yoshizawa, K., Kennett, B., 2002. Determination of the influence zone for surface wave paths. *Geophys. J. Int.* 149, 440–453.
- Zhang, Z., Yang, L., Teng, J., Badal, J., 2011. An overview of the earth crust under China. *Earth Sci. Rev.* 104, 143–166.
- Zhao, J., Yuan, X., Liu, H., Kumar, P., Pei, S., Kind, R., Zhang, Z., Teng, J., Ding, L., Gao, X., Xu, Q., Wang, W., 2010. The boundary between the Indian and Asian tectonic plates below Tibet. *Proc. Natl. Acad. Sci. U. S. A.* 107, 11229–11233.
- Zheng, Y., Shen, W., Zhou, L., Yang, Y., Xie, Z., Ritzwoller, M.H., 2011. Crust and uppermost mantle beneath the North China Craton, northeastern China, and the Sea of Japan from ambient noise tomography. *J. Geophys. Res.* 116, B12312. <http://dx.doi.org/10.1029/2011JB008637>.
- Zhu, R., Xu, Y., Zhu, G., Zhang, H., Xia, Q., Zheng, T., 2012. Destruction of the North China Craton. *Sci. China Earth Sci.* 55, 1565–1587.